FLUIDICALLY RECONFIGURABLE MICROWAVE DEVICES AND OPTICAL SENSORS

by

Tonmoy Bhattacharjee

A dissertation submitted in partial fulfillment of
the requirements for the degree of

Doctor of Philosophy

(Electrical and Computer Engineering)

at the

UNIVERSITY OF WISCONSIN–MADISON

2015

Date of final oral examination: 9/15/2015

The dissertation is approved by the following members of the Final Oral Committee:

Nader Behdad, Associate Professor, Department of Electrical and Computer Engineering
Hongrui Jiang, Professor, Department of Electrical and Computer Engineering
David Anderson, Professor, Department of Electrical and Computer Engineering
Zongfu Yu, Assistant Professor, Department of Electrical and Computer Engineering
Peter Timbie, Professor, Department of Physics

To my grandparents

Lakshmi Rani Devi, late Nani Gopal Bhattacharjee, late Shushila Bhattacharjee and late Sunil Kumar Bhattacharjee

ACKNOWLEDGMENTS

First and foremost, I would like to express my gratitude to my advisors – Professor Nader Behdad and Professor Hongrui Jiang. None of these would have been possible without their guidance and support. I would like to thank Professor David Anderson, Professor Zongfu Yu and Professor Peter Timbie for graciously accepting my request to serve in the doctoral committee and providing valuable feedback to improve the quality of my work. Thanks also goes out to all the staff of the Electrical and Computer Engineering department for their cooperation during the past several years.

During my study, I had the opportunity to be around some smart and wonderful people. A big thanks to all of them – Amin Momeni, Dr. Amir Masoumi, Kasra Ghaemi, Dr. Chien-Hao Liu, Yayha Mohtashami, Ting-Yen Shih, Dr. Bader Aldalali, Dr. Arash Rashidi, Dr. Meng Li, Dr. Xuezhen Huang, Jayer Fernandez, Bahareh Behzadnezhad, Meng Gao, Elham Mohammadi, Hung Luyen and Alireza Ashtiani. Amin, Amir, Kasra, Yahya, Chien-Hao and Ting-Yen – thank you guys so much for many hours of useful discussion and knowledge sharing and also for your help on many occasions.

I am grateful to my parents, Dulal and Shila Bhattacharjee, for sacrificing many things in their lives so that I can reach this point. Special thanks to my younger brother, Chinmoy Bhattacharjee, for his constant support and inspiration. I would also like to thank my parents-in-law, Roy Ramesh Chandra and Krishna Roy, and brother-in-law, Rahul Roy, for their understanding and motivation. Finally, I would like to acknowledge my relatives, friends and well-wishers for their inspiration and blessings.

Last but not least, I would like to specially thank my loving wife, Priyanka Bhattacharjee, for her sacrifice and sincere support during my journey.

DISCARD THIS PAGE

TABLE OF CONTENTS

Page

DISCARD THIS PAGE

LIST OF TABLES

DISCARD THIS PAGE

LIST OF FIGURES

Appendix
Figure Page

Appendix
Figure Page

ABSTRACT

Reconfigurable periodic structures and antennas are in great demand both in the military and commercial areas. A vast amount of research and development work has been done in realizing reconfigurable periodic structures and antennas. Some of the technologies proposed to realize these reconfigurable devices are complex in nature and have high cost involved with them. Therefore, their use is mostly limited to the military sectors and these devices have not been used in many commercial systems. In this thesis, a significant portion has been dedicated to provide innovative, interdisciplinary and cost-effective solution to realize reconfigurable microwave devices that could potentially enable development of affordable future wireless systems, which can also handle high-power signals without compromising the performance of the overall system.

Fluidically reconfigurable periodic structures and antennas based on a liquid varactor concept with a new tuning technique are presented and discussed in this thesis, which show promise in developing microwave devices that are cost-effective and capable of handling high power. The technique is expected to minimize the complexity of the system and enable widespread use in high-power applications. The proposed fluidically tunable periodic structures and antennas consist of a 3D printed substrate with embedded hollow channels. The hollow channels are then populated with metal/glass balls and/or metal cylinders. The layout of the channels is designed in a fashion that can distribute pressure evenly causing the balls and/or cylinders inside the channels to move synchronously or just be controlled independently of each other.

The suggested design for these microwave devices does not use any type of electronic component to achieve reconfigurability and therefore makes them feasible to be used in high-power applications.

Chapter 1

Introduction

1.1 Motivation

The reconfigurability of periodic structures and antennas is increasingly becoming an active area of interest both in academia as well as in the commercial world. Even though the use of reconfigurable periodic structures and antennas in the military sector dates back to several decades, their use in the commercial world has rather been limited due to the complexity and affordability involved with them. Real time tuning of periodic structures and antennas has plenty of advantages such as controlling performance based on need, reducing overall size of devices, making energy-efficient devices and developing cost-efficient products. A periodic structure is an assembly of identical elements arranged in 1-D or 2-D lattice. Periodic structure is a well-known and matured topic. Significant amount of work has been done with periodic structures over the past several decades [1] - [5]. They have numerous applications in the RF and Microwave area including design of metamaterials [4], frequency selective surfaces [5]-[7], reactive impedance surfaces [8] and antenna arrays [9]. A reconfigurable antenna is an antenna in which the operating frequency, impedance bandwidths, polarizations and radiation patterns are changed to accommodate changing operating requirements. Plenty of work has also been done on reconfigurable antennas and can be found in the literature [10].

Over the course of time, there has been a spike in demand for multi-functional and sophisticated systems in commercial as well as government, military predominantly, arenas. For example, in the military domain frequency selective surfaces, a type of spatial filter, are used

in various stealth applications. With rapid technological developments, enemy systems are becoming more sophisticated and capable of detecting stealth entities. In the commercial world, over the past decades a dramatic growth in wireless communication has been observed especially with the introduction of smart phones and tablets. The number of smart phone and tablet users is increasing rapidly not only in developed countries but also in the developing countries. As the number of consumers is increasing, so is the appetite for more data. This demand has driven the introduction of various types of wireless standards such as 2G, 3G, 4G etc. Each generation of wireless standards provide higher data rates from their previous one. In addition to this, there is also an affinity for relatively small and/or compact products among the consumers. On the other hand, there also exists constraints on the available radio wave spectrum. Not all available spectrum can be used for all the types of wireless applications. Some spectrums are allocated for military use only whereas some are allocated for commercial use. Therefore the available spectrum has to be judiciously used in order to get maximum output. Besides these, energy efficiency and high-power handling capability are of also a great concern based on the type of applications. Due to all of these factors, the demand for reconfigurable periodic structures and antennas possessing agile frequency responses as well as the ability to withstand incoming high-power signals is on the rise.

Noticeable amount of work has been done in developing tunable periodic structures and antennas. By far, the most commonly used method to achieve tunable structures is the integration of some sort of electronic devices such as varactors, micro-electromechanical systems (MEMS) switches, diodes, liquid crystals, liquid substrates and so on. All of these electronic components also need some sort of power supply network for operation, control and also isolate RF power that can possibly damage the components. This adds complexity to the overall structure, makes it difficult to assemble and also bulky in size. For large-scale tunable periodic structures, it becomes imperative to incorporate electronic components into each unit cell which further complicates their design. Moreover, the biggest trade-off for these periodic structures seems to appear when they are intended to be used in high-power applications. At

high-power levels, electronic devices become non-linear, an inherent behavior, and the performance of overall structure degrades drastically. In order to circumvent some of the problems associated with the use of electronic components, liquid substrates, liquid metals and liquid crystals are used to realize tunable periodic structures. However, these techniques either have been demonstrated in unit cell level or also require some type of networks to supply power and to control the operation.

Unique and well-proven ideas related to antennas with reconfigurable parameters such as frequency, polarization and beam direction can be found in the literature. For example, an antenna with single resonant frequency can be easily tuned using various electronic components as described for tunable periodic structures. Then by modifying the physical and/or electrical properties of a single resonant antenna, it can be made a dual or triple band antenna which in turn can also be tuned over a certain frequency band of operation. This has been successfully accomplished for various types of antennas [10]. Some of the ideas has already been implemented and have found applications in commercial as well as in military sectors. Beside the frequency reconfigurability of an antenna, the beam direction of the antenna can also be steered to different directions.

The prominent technique used to steer the beam of an antenna or an array of antennas is the use of phase shifters. Traditional phased array antennas can be categorized into either active or passive arrays depending on the specific system architecture. A passive electronically steered array (PESA) has a central transmitter and receiver with phase shifter included at each radiating element of the array. On the other hand, for active electronically steered array (AESA) a transmitter/receiver (T/R) module is used for each radiating element. Each T/R module is a fully developed transceiver that can not only amplify the transmitted and received signal but also control the phase and amplitude of these signals to achieve beam steering. However, both AESAs and PESAs have their own limitations. For PESAs, it is the loss introduced by the feeding network and the phase shifters whereas for AESAs, it is the cost involved with T/R modules. These limitations have created an obstacle for widespread use of AESAs and PESAs in various applications especially in the commercial world. Due to these, there have

been efforts to reduce the number of phase shifters or eliminate them which in turn has created a new type of phased array known as Electronically Steerable Parasitic Array Radiator (ESPAR). With this technology, the use of phase shifters has been limited by using mutual coupling between adjacent radiators and loading the radiators with tunable reactances which create the necessary phase shift to steer the beam. However, as usual, electronic components are used predominantly to achieve beam direction reconfigurability.

Therefore, the motivation of this thesis is to investigate and develop a technique to tune a periodic structure with multiple unit cells and antennas without the use of any type of electronic device and/or additional bias network. In this thesis, a new technique has been presented and discussed that has the potential for developing affordable and electronic component-less reconfigurable large-scale periodic structures and antennas. It should be pointed out here that when the term antenna is used it can indicate any type of antenna such as dipole, loop, patch, slot and so on. However, in this thesis the discussion is limited to only patch antenna or patch antenna arrays.

So far, the earlier discussions have primarily been focused on reconfigurability of microwave devices. During the course of accomplishing the research goals of this thesis, a discussion session with an organization and Prof. Jiang and Prof. Behdad has led to the pursuit of developing a miniaturized sensor for water hardness detection and determination. Moreover, the feasibility of sharing some resources between the sensor and reconfigurable microwave devices projects has generated further interest to investigate this development idea. The proposed design and experimental results have been finally published in the IEEE Sensors Journal. This paragraph presents a short introduction of the different topic i.e. water hardness detection sensor and a detailed discussion is included in the appendix section of this thesis. Water hardness affects people in households as well as commercial entities. Hard water creates spots in utensils, toilets and bathtubs and degrades performance of the machinery and cleansing products in households and commercial installations. Household consumers and businesses spend lots of money to remove hardness from water. Currently, there are products to detect and determine

water hardness that can range from few hundred to several thousands of dollars [11] - [13]. Besides the cost of these products, their use can be time consuming, complicated and require constant monitoring. For big businesses it might be feasible to buy expensive equipment to detect and determine water hardness with dedicated personnel continuously monitoring the detection system. However, for household consumers it is not always possible to afford an expensive system and continuously monitor it. Aside from commercial product development, a noticeable amount of research work has also been done in devising techniques and/or apparatuses to detect and determine water hardness [14] - [23]. Nonetheless, converting those ideas/works into cost-effective products may not be feasible and not easy to use in average households. Therefore, the motivation behind this effort is to investigate ways to develop a water hardness (total hardness) detection and determination mechanism that will be cost-effective, robust and easy to use. It is by no means intended to replace existing techniques/methods/products and precisely determine hardness in water. It would rather be used as a secondary means to detect water hardness and provide consumers a cost-effective solution and a judicious use of their primary/existing systems and their resources.

1.2 Proposed Approach

As stated in the previous section, tunable periodic structures and antennas have been realized using electronic media such as switches, varactors and so on. 'Electronic tuning' is a preferred choice because of its fast tuning feature. However, with the fast tuning feature several limitations also arise such as non-linearity, limited power handling capability, a bias voltage supply and protection circuitry. In order to overcome all the above mentioned issues, our group has recently proposed the use of 'fluidic tuning' technique that eliminates issues associated with 'electronic tuning'. With this concept, a liquid metal slug, Galinstan — a eutectic alloy of gallium, indium and tin, is embedded in Teflon tubes and strategically placed in a periodic structure composed of sub-wavelength capacitive patches and inductive grids. The Galinstan slugs are moved by applying pressure through syringes in order to tune the response of the reactively loaded periodic structure. This effort is experimentally verified and good agreement

was observed with simulated results. It was also observed from simulation that these types of structures can withstand high power levels. However, this was implemented in a unit cell level and assembling multiple unit cells proved to be extremely difficult. Therefore, a new technique is proposed that enables synchronous tuning of a periodic structure consisting of multiple unit cells using the same principle of fluidic tuning proposed by our group. This technique does not only enable the tuning of multiple unit cell based periodic structures but also eliminates the use of liquid metal slugs with solid metal and glass balls, which are also easy to handle. The 'fluidic tuning' technique is then applied to a rectangular patch antenna and antenna array to achieve a tunable dual-band response and beam steering in the H-plane respectively.

Three-dimensional (3D) printing or additive manufacturing is a rapidly emerging technology. Recently strong interest in using this technology has been observed in different fields ranging from art to engineering. Moreover, rapid advancement in developing efficient printers and variety of materials used to print objects has made it possible to print 3D objects fast and at a reasonable price. Therefore, in the above mentioned efforts 3D printing is used to build substrates with embedded channels for the periodic structures/antennas as well as the sensor prototype for water hardness detection. There already exists different computer-aided design tools such as SolidWorks to model any 3D object which can then be easily realized with the help of a 3D printer. Using 3D printing technology to build prototypes also turned out to be a cost-effective solution for the works presented in this thesis.

1.3 Literature review

From the discussion in the earlier sections, the goal of this thesis is to examine a new technique to fluidically tune multi-unit cell periodic structures and microstrip antennas. Before delving into the technique used to reconfigure multi-unit cell periodic structures and antennas, a brief literature review is offered on these technologies and the progress that has been made in making them tunable. In the following subsections, a literature review on periodic structures is presented followed by dual-band patch antenna, beam steerable patch antenna and finally various tuning mechanisms applied to these microwave devices.

1.3.1 Periodic Structures

Periodic structure is an assembly of identical elements arranged in 1-D or 2-D lattice. It has many useful applications in various areas of electromagnetics such as phased arrays, electromagnetic band gap structures and reflectarrays [24]. It also has unique properties that can be used to increase antenna performance, electromagnetic propagation and electromagnetic absorption [24]. Due to its unique and promising properties, research interest in the area of periodic structures is still strong. Plenty of novel ideas in developing various types of these structures are proposed and can be found in the open literature. For example, frequency selective surfaces (FSS), a type of periodic structure, has been extensively studied since the early 1960s. FSSs act as a type of a spatial filter. They have been extensively studied and used in different applications such as metallic radomes [25], reflectors [26], phase screens for beam steering [27], and electromagnetic shielding [28]. FSS can be typically categorized into resonant and non-resonant types based on the variety of elements used in each unit cell. A non-resonant type FSS is generally a two-dimensional periodic arrangement of sub-wavelength patches or wire grids whereas a resonant type FSS is composed of resonant type elements within each unit cell. FSSs consisting of non-resonant elements exhibit behavior corresponding to low-pass or high-pass filter depending on whether a capacitive or inductive surface impedance sheet is used. On the other hand, resonant type FSSs use resonant elements such as dipole or slot. FSSs consisting of dipole-type elements exhibit band-stop frequency responses at their first resonances, while slot-type elements exhibit band-pass frequency responses. However, FSSs containing resonant elements have some limitations such as increase of structure thickness for sharp frequency responses, increase in sensitivity to oblique angle of incidences and so on [29]. To overcome some of these problems, a new type of FSS known as miniaturized-element frequency selective surface (MEFSS) has been proposed and extensively studied by various research groups [29]. MEFSSs are periodic structures with sub-wavelength dimensions of unit cells that are less than $\lambda_0/4 \times \lambda_0/4$, periods and consisting of non-resonant constituting elements (unit cells) [29]. The main advantage of this type of FSS is reduced unit cell size and overall reduced thickness. Besides FSSs, another type of periodic structure is high impedance surfaces. High impedance

surfaces have some unique characteristics such as not supporting propagating surface waves and reflecting electromagnetic waves with no phase reversal [30]. Generally they are made of continuous metal and conduct DC currents. However, they do not conduct AC currents within a forbidden frequency band. These unique electromagnetic structures have application in variety of electromagnetic problems including new kinds of low-profile antennas [30].

1.3.2 Dual-Band Patch Antenna

A patch antenna is a popular microwave device for its attractive features such as low-profile, light weight and compatibility with monolithic microwave integrated circuits (MMIC). Due to its well-known features, it has found applications in a variety of modern communication systems. It has been extensively studied and a detailed analysis of its operation can be found in the literature. In spite of patch antenna's convenient features, it has some drawbacks such as narrow bandwidth, relatively low efficiency, unwanted radiation from feed network and so on. However, in applications where larger bandwidth is critical, multi-frequency response is desired and space is constrained, patch antenna operating in multiple frequencies has advantages compared to other planar antennas. Dual-frequency patch antennas exhibit dual-resonant behavior in a single radiating element [31]. Due to the demand and promise that dual-band patch antenna holds, extensive research has been done to come up with novel ideas to make a single resonant antenna structure operate at dual-frequencies. These ideas vary from modifying the physical geometry of the antenna itself to reactively loading the structure. For example, in [32] two bent slots are placed close to the non-radiating edges of a rectangular patch which result in a dual-frequency behavior of the antenna. Similarly slots of different shapes can be strategically placed in a patch to achieve a dual-band response [33]. Beside modifying the antenna's geometry, a reactive loading technique can be used to make a single resonant antenna exhibit dual-band response. For example, a simple way to achieve a dual-band response is to connect a stub to one radiating edge in a way that introduces an additional resonant length responsible for the second operating frequency [31]. Other prominent techniques used in achieving a

dual-band response are by means of using multiple radiating elements where each of them will support strong currents and radiation at the resonance and by utilizing orthogonal modes [31].

1.3.3 Tuning Mechanism

Different tuning techniques have been explored by researchers to tune the responses of periodic structures that are in the form of frequency selective surfaces (FSS) [34] - [39], microwave lenses [40] - [42], microstrip structures [43] and so on. C. Mias has proposed a tunable frequency selective surface that consists of vertically and horizontally positioned convoluted dipole elements [34]. Each dipole element contains a varactor diode and biased via a resistive-lumped-element biasing grid that suppress undesirable resonances and improve filter's low-pass response. The FSS contains multiple unit cells and the tuning idea is experimentally verified. However, the limitation of the work is in its use of varactor diodes, resistive elements, resonant structures i.e. dipole elements and bias networks. For high-power applications, none of these items are desired and cause performance degradation. Then, W. Hu *et al.* has presented a frequency selective surface which exploits the dielectric anisotropy of liquid crystals to generate an electronically tunable bandpass filter response at D-band (110-170 GHz) [36]. A bias voltage of 10 V is applied to orient the liquid crystal molecules and change the permittivity of the substrate. That way, the frequency response of the FSS is manipulated. Besides these, use of tunable MEMS capacitors have demonstrated the ability to eliminate intermodulation distortion and losses compared to those of varactor diodes [40]. The complicated fabrication process is the main drawback for the MEMS based tunable lens. Tunable lenses that use ferroelectric dielectrics to achieve tuning have been proposed to reduce the number of phase shifters (required to achieve beamforming) [42]. Such tunable lenses made of ferroelectric dielectrics can possibly lead to low-cost and high-power phase arrays. However, DC biasing is required for the ferroelectric material along each column of the lens. M. Li *et al.* has proposed a new technique to tune periodic structures with the help of fluid [38] - [39]. It does not use any electronic components, bias networks or even liquid substrates that require a voltage supply to operate. However, the technique is applied to only a unit cell structure. B. J. Lei *et al.* has

proposed a wideband liquid tunable frequency selective surface that primarily consists of periodically spaced PTFE tubes that are pressure-driven and filled with mercury (Hg) and mineral oil [44]. 'Hg' is an extremely toxic element and its use in any application is very risky.

For antennas, in this case patch antennas, a similar type of previously described methods are used to tune their frequency responses [10]. In a paper authored by Y. J. Sung, a varactor diode is placed on a small gap between a square patch and a parasitic strip [45]. This results in a dual-band antenna and by varying the diode value, the frequency response of the antenna is tuned. Then in another paper authored by Y. X. Guo *et al.*, a compact dual-band patch antenna is proposed which is realized by using slot-loading and short-circuited size-reduction techniques [46]. In this antenna, by controlling the short-plane width the resonant frequencies are tuned with a frequency ratio of $\approx$ 1.6 - 2.2. J. Liang and H. Y. David Yang investigate a tunable metamaterial in integrated circuit structures through an example of a microstrip patch antenna on a mushroom-type EBG structure [47]. Dual-frequency operation of an equilateral-triangular patch antenna is achieved by loading a pair of slits in the patch and using two PIN diodes to switch the slits on or off [48].

For beam steerable antennas, the prominent technique used to achieve beam steering in a desired direction is the use of phase shifters. Therefore, these beam steerable antennas are also referred to as phased-array antennas. Extensive research and development work has been done in phased-array antennas and early work dates back to the early 1920s and 1930s [49]. However, cost associated with the development and implementation of phased-array antennas has restricted their use in all communication systems. Therefore, there has been a surge in interest to develop technologies that will make phased-arrays affordable and their use more widespread. One such example is taking advantage of mutual coupling among parasitic elements and then using switching components in the system or feeding each element separately [50]. The elements in the parasitic array system can be oriented in the E-plane and/or H-plane in a 2-D fashion or even stacked on top of one another. A detailed description of various configurations of these parasitic array systems can be found in [50]. Plenty of research has also been done to come up with unique ideas for developing these mutually coupled patch array system. For

example, a type of antenna closely related to switched parasitic antennas has recently received some attention, which is known as Electronically Steerable Parasitic Patch Array Radiator (ESPAR). In ESPARs, phase shifting is achieved by mutually coupling adjacent parasitic radiators and loading them with tunable reactances at the terminals. This phase shifting causes the beam to steer to the desired direction. In a work reported by J. J. Luther *et al.*, initially two parasitic patch elements are mutually coupled to a center patch [51]. Then varactors are loaded between the center element and parasitic elements as well as separately along the non-radiating edges of the parasitic elements. By changing the varactor values, beam steering of $\pm 15^{\circ}$ is obtained with consistent gain, sidelobe level and overall beam shape.

1.4 Thesis Overview

The aim of this research is to investigate and implement techniques that will enable tuning of large-scale periodic structures and antennas. The efforts undertaken to accomplish the research goal have been composed and presented in detail in several chapters of this thesis. A brief overview of each chapter follows in the later subsections.

1.4.1 Chapter 2

In this chapter, a technique to fluidically tune the responses of periodic structures with multiple unit cells and finite dimensions is presented. The periodic structures are composed of sub-wavelength constituting unit cells. This technique is applied to a two-dimensional high impedance surface with multiple unit cells and the response of the structure is continuously tuned. The technique is based on embedding metal and glass balls inside several parallel channels within a dielectric substrate supporting the structure. In each channel, a periodic arrangement of metal and glass balls is assembled and is allowed to move freely within the channel. By moving this periodic train of balls over small distances with respect to the fixed periodic structure, the response of the structure is continuously tuned. 3D printing technology is used to implement the dielectric substrate with embedded fluidic channels. An architecture for the fluid distribution network is proposed that ensures the movement of balls in all channels is

synchronized. A prototype with 16 parallel channels accommodating several unit cells in each channel is fabricated and synchronized movement of the balls is verified experimentally when the balls in channels are embedded in mineral oil and pressure driven. Using this substrate and an array of sub-wavelength capacitive patches fabricated on a thin dielectric substrate, a fluidically tunable high-impedance surface is designed and experimentally characterized.

1.4.2 Chapter 3

In this chapter, a new technique for designing a dual-band patch antenna with closely-spaced bands of operation, whose response can be changed dynamically using a fluidic tuning mechanism is presented and discussed. Using this technique, a dual-band tunable patch antenna operating at around 2.5 GHz is designed and fabricated using 3D printing. Two oil-filled channels are placed in the substrate of the antenna along the non-radiating edges of the patch and filled with movable metal cylinders. As the cylinders are introduced underneath the patch, it starts to exhibit a dual resonant behavior with both resonances having a similar electric current distribution. The separation between the two resonant frequencies is a function of the relative position of the metallic cylinders underneath the patch antenna. As the overlap volume between the metal cylinders and the patch increases, the frequency of the first band, f_1, starts to decrease and that of the second band, f_2, increases. The maximum separation between f_1 and f_2 is achieved when half of the lengths of the metallic cylinders are underneath the patch. The prototype device designed in this work can achieve frequency ratios in the range of f_2/f_1= 1.08 - 1.30. The antenna demonstrates similar radiation characteristics at both bands of operation.

1.4.3 Chapter 4

In this chapter, a technique for designing a parasitic patch antenna array whose beam can be steered dynamically using a fluidic tuning mechanism is presented. Using this technique, a 3-element patch antenna array operating at around 5 GHz is designed and fabricated using 3D printing. Two oil-filled channels are placed in the substrate of the antenna along the radiating edges of the patches and filled with movable metal cylinders and glass balls. The parasitic

elements are mutually coupled to the center element in the H-plane. As the train of metal cylinders and glass balls are moved left or right - with respect to the center driven patch element, the beam is steered toward the opposite direction. The proposed parasitic patch array is able to steer the beam $\pm 22.5^{\circ}$ with maintained impedance matching.

1.4.4 Chapter 5

In this chapter, power-handling capability of the proposed fluidically tunable periodic structure and patch antenna is briefly presented. EM-Thermal co-simulations are performed to verify the amount of power these structures can handle without burning or melting. Analysis is done for both continuous wave and transient power-handling capabilities of these structures. The results of these simulations are provided and briefly discussed in this chapter.

Chapter 2

Large-Scale Fluidic Tuning of Sub-wavelength Periodic Structures

2.1 Introduction

Periodic structures have numerous applications in the RF and Microwave area including the design of metamaterials [4], frequency selective surfaces [5]- [7], reactive impedance surfaces [8], and antenna arrays [9]. In recent years, with the emergence of the field of metamaterials, sub-wavelength periodic structures have received a significant amount of attention. As the use of multi-functional and sophisticated systems both in the commercial and in the military arenas is becoming prevalent, the demand for reconfigurable periodic structures possessing agile frequency responses is on the rise. In the past, different techniques have been explored for designing tunable periodic structures. By far, the most widely used technique for making tunable periodic structures is to integrate electronically tunable elements such as solid state or MEMS varactors with the unit cells of the periodic structure [34]. This technique, however, is rather challenging to implement in a physically large periodic structure with sub-wavelength constituting elements. In such a structure, in a relatively small physical area, hundreds or even thousands of unit cells may be packed which makes the task of integrating active devices with them impractical. Other techniques have also been examined for making periodic structures tunable. Among these, using liquid substrates [35], liquid crystals [36], and magnetic MEMS devices [37] can be mentioned.

Recently, our group proposed a new fluidic tuning technique for designing tunable periodic structures with sub-wavelength periodicities [38]- [39]. This technique does not rely on

using any electronic devices and eliminates the need for using biasing networks or individually integrating active elements with each unit cell of the periodic structure. The technique is based on embedding capillary tubes filled with liquid metal droplets within a periodic structure composed of sub-wavelength capacitive and/or inductive impedance surfaces. By moving the liquid metal droplets within the unit cell of the structure the capacitance values of the capacitive surface impedances can be changed in a continuous fashion very much like what is done using electronic varactor [39]. Using such liquid varactors, tunable miniaturized-element frequency selective surfaces were designed and experimentally demonstrated at the unit cell level. It was demonstrated that the frequency responses of such tunable FSSs can be continuously tuned over a very wide bandwidth. It has been also shown that this class of tunable FSS is expected to be capable of handling significantly higher transient power levels as it does not use electronic devices that are inherently nonlinear [39]. The aforementioned studies examining liquid-tunable FSSs focused on characterizing the tuning capabilities of such structures at the unit cell level [38]- [39]. However, in a large tunable periodic structure, multiple unit cells exist and they have to be controlled simultaneously. Therefore, suitable implementation techniques need to be developed for expanding this tuning technique from the unit cell level to a large panel level. Specifically, we experimentally found out that using the liquid metal Galinstan in a liquid Teflon solution, a unit cell of a periodic structure can be tuned relatively easily. However, assembling trains of liquid Galinstan droplets and driving them synchronously to emulate multiple unit cells proved to be extremely challenging in the laboratory. Galinstan oxidizes rapidly in air and wets almost any surface [52]. Moreover, when trains of liquid metal droplets were assembled in a capillary tube, maintaining the spacing between two consecutive liquid metal droplets proved to be impractical when the entire system was pressure driven. Beside the use of Galinstan, an FSS consisting of periodic array of liquid mercury (Hg) droplets separated by gaps of mineral oil contained in an array of PTFE tubes was also presented [44]. However, mercury is an extremely toxic substance and its use is not practical in real-life systems.

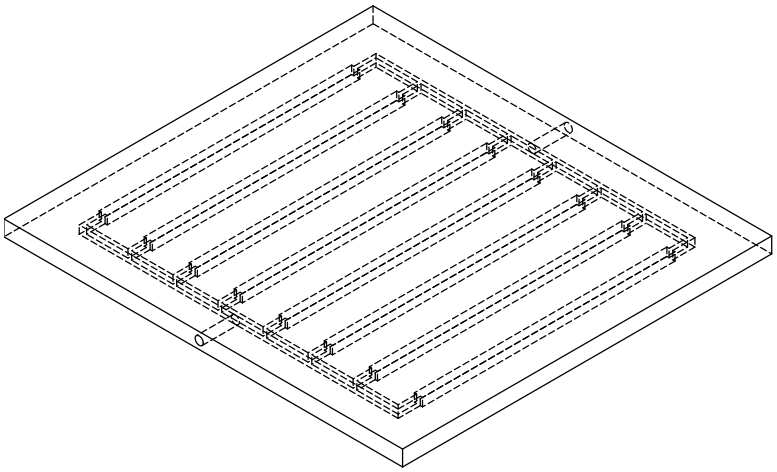

(a)

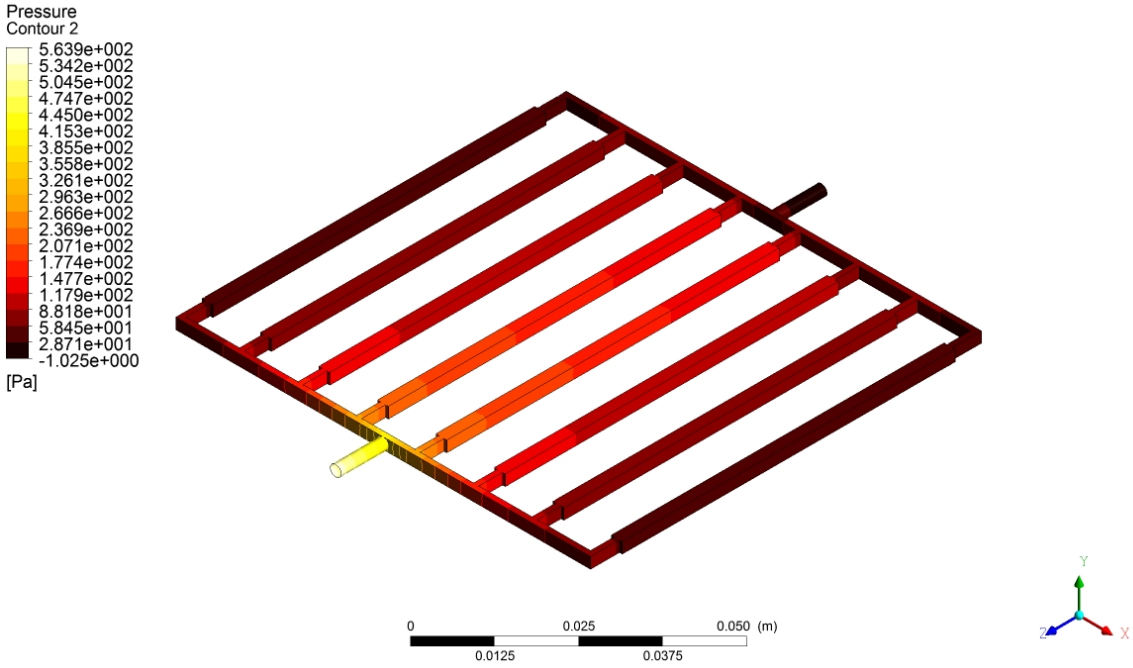

(b)

Figure 2.1: (a) Topology of a slab with 8 fluidic channels (b) Pressure distribution among the channels verifying asynchronous fluid movement.

In this chapter, we propose a new implementation technique for realizing fluidically tunable periodic structures that operates based on the same principles of operation as the Galinstan-tunable FSSs reported in [39]. Unlike the structures reported in [38] and [39], however, the demonstration of the fluidically-tunable structure presented in this work is not done at the unit cell level. Specifically, this structure has multiple unit cells in a two-dimensional periodic structure and achieves synchronous tuning of all the unit cells using the proposed fluidic tuning technique. Moreover, this new implementation technique does not use Galinstan or any liquid metals. Instead a series of circular chrome steel and glass balls are used to replace the liquid metal slugs and the dielectrics separating them. These solid, non-toxic but movable metal balls can be easily handled and arranged to emulate a train of liquid metal droplets with fixed periodicity and spacing between each droplet. Additionally, with the new implementation technique, we also eliminate the use of any type of capillary tubes and replace them with a 3D printed dielectric slab containing multiple embedded parallel channels capable of accommodating numerous unit cells.

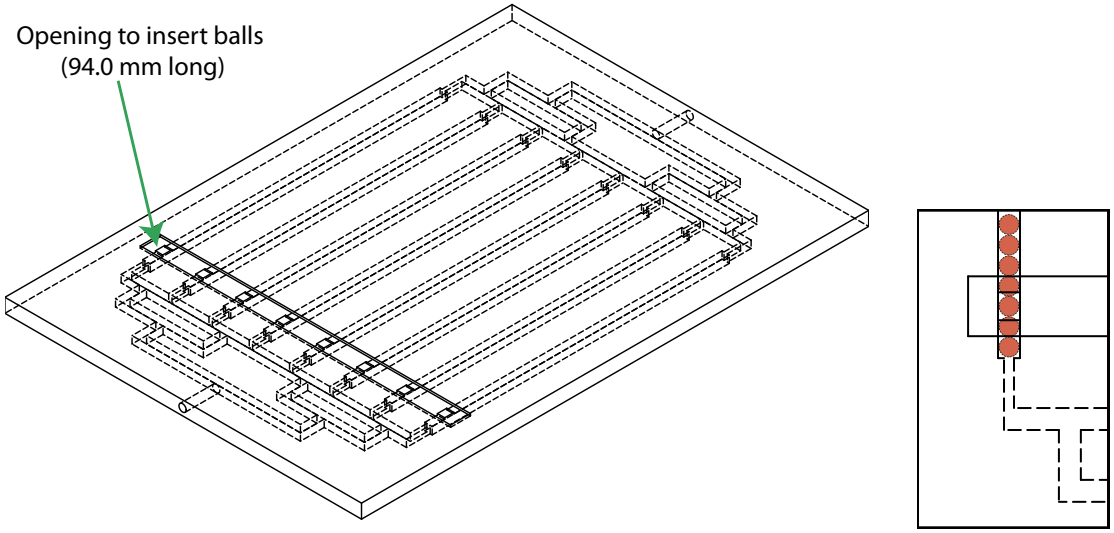

Figure 2.2: (a) Topology of a 3D printed substrate with 8 fluidic channels (b) Zoomed in view with balls inside one channel [Top View].

2.2 Design Procedure and Simulation

In our initial design we primarily focused on designing a device that eliminates the use of tubes and liquid metal slugs and investigate how to move several periodic trains of metallic and glass balls in multiple channels synchronously. A slab consisting of 8 parallel channels was designed using a CAD tool, SolidWorks, as shown in Fig. 2.1(a). Channels of smaller cross sections are placed in between the longer channels and the channels connecting the inlet/outlet to prevent the balls from exiting their dedicated channels. The structure is simulated using ANSYS Fluent to verify synchronous movement of fluid inside the channels. Simulation result shows that fluid starts to move in to the channels close to the inlet first and then gradually move to the subsequent channels as shown in Fig. 2.1(b). Therefore, the layout of the channels is not a suitable choice to carry fluid in a synchronous fashion. Then a new layout consisting of channels laid out in branch network fashion is employed as shown in Fig. 2.2(a). The structure is simulated using ANSYS Fluent and simulation result shows evenly distributed pressure among all the channels as shown in Fig. 2.3. The channel dimensions are 2.2 mm $\times$ 2.2 mm $\times$ 90.0 mm. Eight 1.0 mm $\times$ 2.2 mm $\times$ 5.0 mm channels are placed between the 90.0 mm long channels and the branch networks. A 94.0 mm long opening is placed on one face of the slab so that metal and glass balls can be easily inserted into the channels and is sealed off with a 3D printed thin strip and epoxy. The overall slab has dimensions of 108.0 mm $\times$ 4.2 mm $\times$ 153.6 mm.

Then a prototype is printed using a Viper Si2 3D printer from Wisconsin Discovery Institute at the University of Wisconsin Madison. The printer uses Accura 60 - a type of photopolymer resin - as the printing material, and stereo lithography technique to cure the resin to build the 3D model. After the prototype is fabricated, trains of metal and glass balls are created inside the channels in an alternate fashion as shown in Fig. 2.4. Each train of metal balls and glass balls consists of 5 metal balls and 5 glass balls respectively which are 2.0 mm in diameter. Then two blunt needles are inserted through the inlet and outlet and sealed off with epoxy to prevent movement and leakage of liquid. Using an inlet, the channels are filled up with mineral oil using a 5 ml syringe. After all the channels are filled up, the outlet needle is assembled

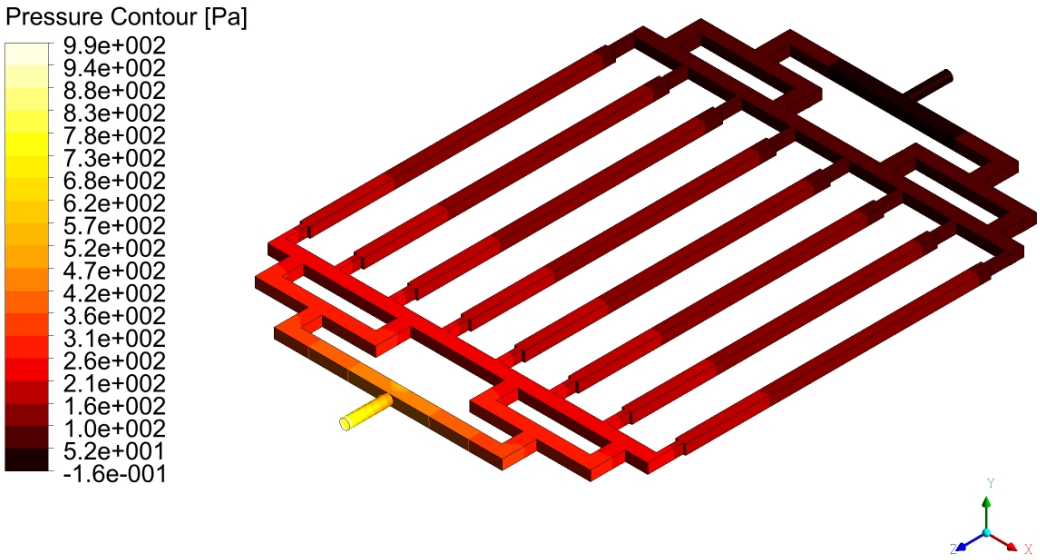

Figure 2.3: Pressure distribution among the channels of the substrate shown in Fig. 2.2.

with a 5 ml mineral oil filled syringe. As one of the syringes is pushed, the trains of metal and glass balls are observed to move in a synchronous fashion. This process was found to be repeatable after multiple back and forth movements of the balls within the channels. Therefore, using the slab with parallel channels and branched pressure distribution network is an effective technique to achieve synchronous movement of periodic objects in multiple channels for large-scale fluidically tunable structures.

2.3 Design of a Fluidically-Tunable Reactive Impedance Surface

The 8 channel prototype we built demonstrated that synchronous movement of metal and glass beads can be achieved for a periodic structure panel consisting of multiple unit cells. To study the use of this tuning concept in designing tunable periodic structures, the 8 channel design was scaled to a 16 channel one, which would be then integrated with a periodic arrangement of sub-wavelength capacitive patches to obtain a tunable reactive impedance surface (RIS). The 3D printed substrate is sandwiched between the array of patches and a ground

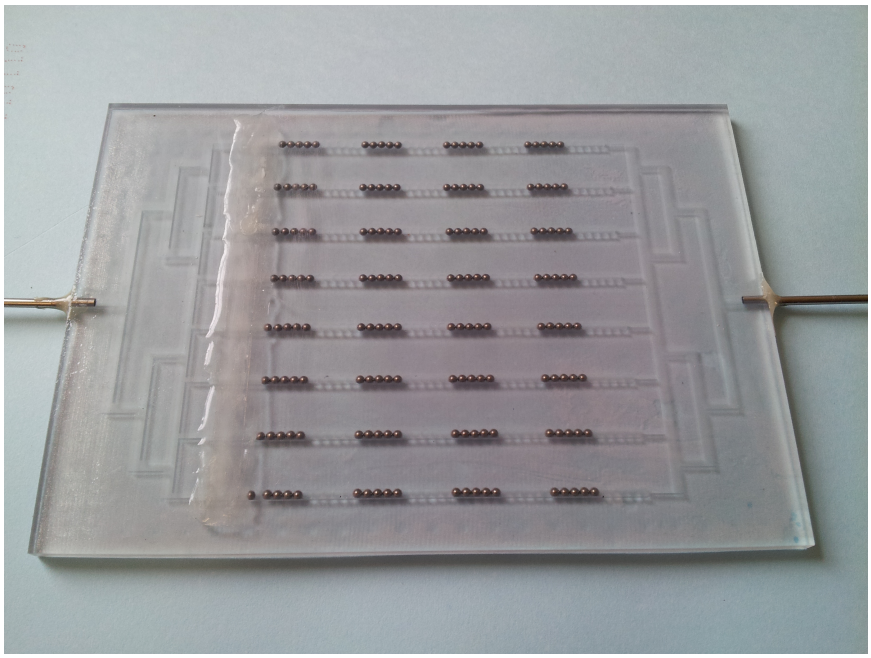

Figure 2.4: Photograph of a fabricated prototype of the structure shown in Fig. 2.2 with periodic trains of metal and glass balls embedded in all channels.

plane. The capacitive patch array is fabricated on a 5 mils-thick Rogers 5880 laminate. Preliminary simulation of a unit cell of this structure was performed using CST Microwave Studio to evaluate its tuning capability. It was found out that a structure with a unit cell size of 7.0 mm with an overall substrate thickness of 2.32 mm can provide 1.5 GHz of tuning range. The 3D printed substrate thickness was chosen by taking into account the minimum dimensions of the channels that the 3D printer can accurately fabricate. The unit cell had 6 metal balls and 1 glass ball all with a diameter of 1.0 mm (see Fig. 2.5(a)). The metal balls are modeled as PEC and the glass ball is modeled as a dielectric with ϵ_r = 6.9 [53]. With regards to the conductivity of the metal balls, as discussed in [39], the specific conductivity is not very important as long as the conductivity is high enough to create significant fringing fields in the capacitive gap areas. For dielectric balls, it is desired to have low dielectric constant values. The gap between the two adjacent capacitive patches was 2.4 mm, which was determined based on the design guidelines mentioned in [39]. The position of each ball was moved one at a time and the phase

of the reflection coefficient was recorded to evaluate the tuning range. The unit cell configuration of 2.5(a) gives the response shown in Fig. 2.5(b). As the balls move, the phase change occurs gradually and eventually provides the response shown in Fig. 2.5(c), when the glass ball is underneath the gap. Fig. 2.6 shows the photograph of the 3D printed dielectric substrate

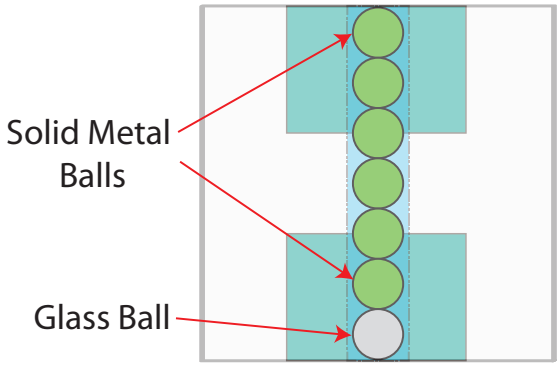

(a)

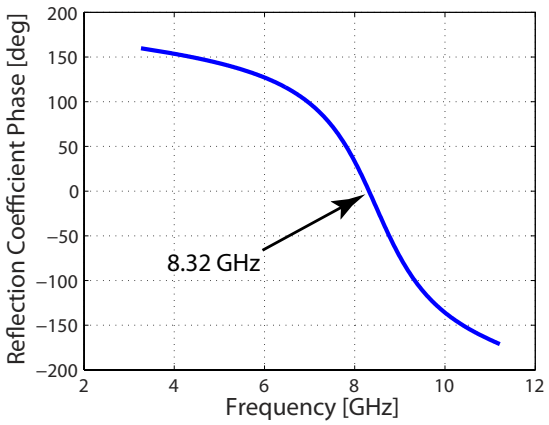

(b)

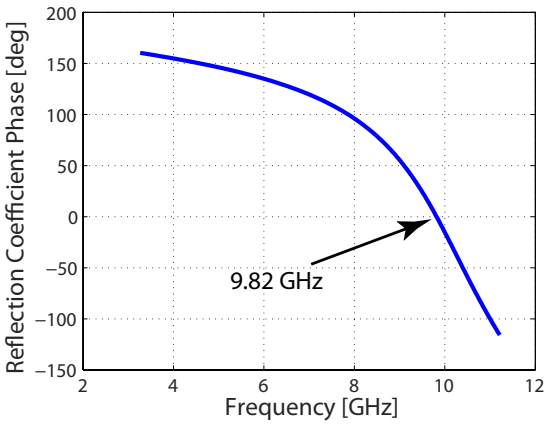

(c)

Figure 2.5: (a) Unit cell of one embodiment of the proposed tunable reactive impedance surface [Back View]. This structure has unit cell dimensions of 7 mm $\times$ 7 mm and uses seven balls per unit cell to achieve tunability (b) Simulated phase response when the metal ball is underneath the gap and (c) Simulated phase response when the glass ball is underneath the gap of capacitive patches.

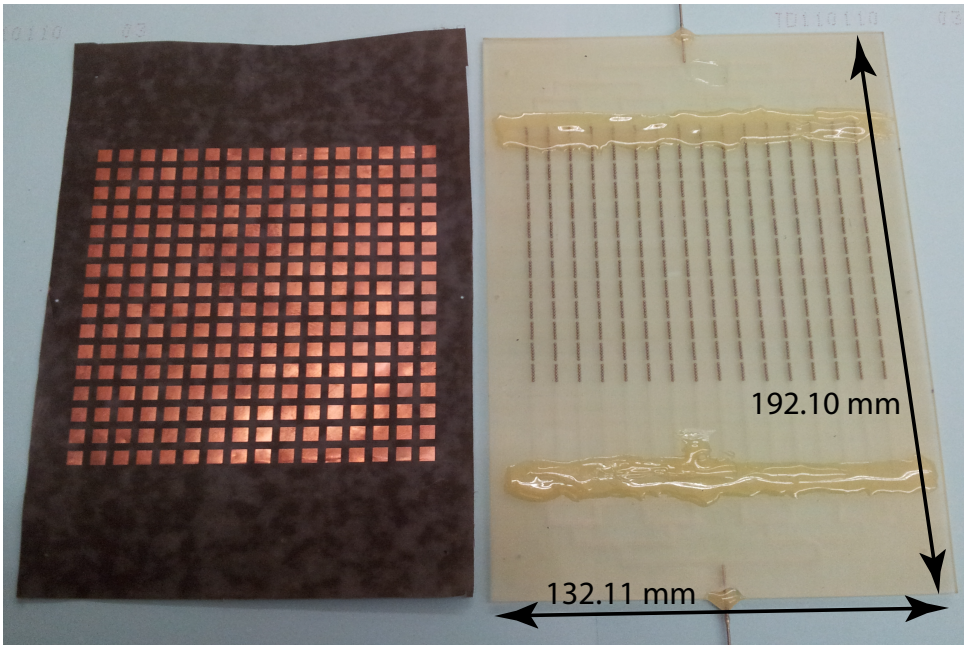

Figure 2.6: [Left] Photograph of the capacitive patch array fabricated on a 5-mils thick Rogers 5880 laminate, [Right] 3D printed slab with 16 fluidic channels populated with metal and glass balls (structure with 7.0 mm unit cells).

with 16 embedded fluidic channels printed by Agile Manufacturing Inc. of Ontario, Canada. The printing material used to build the structure was VisiJet MX. It is a semi-transparent material and softer compared to Accura 60. Each ball was inserted into the channels one at a time by hand and the dimensions varied between 0.97 mm to 1.03 mm due to manufacturing imperfection at that size. The channels in the printed structure had a tolerance of 25% which was intentionally included in the design for easy clean up of the residues of support structures built by the printer during the printing process as well as for the easy movement of the balls inside the channels. Before covering one side of the printed slab with a ground plane and the other side with a periodic array of sub-wavelength capacitive patches, the outlets on two sides were sealed off with blunt needles. The inside of the channels were then filled with mineral oil using 10 ml syringes. As one of the syringes was pushed, the trains of metal and glass balls started to move but not in a synchronous fashion as observed with the 8 channel prototype.

Several attempts were made to achieve complete synchronization among the 16 channels but were not successful. Close observation has revealed the inside walls of the channels were not completely smooth and presence of wax residues. Wax is used as a support material for the channels during the 3D printing process. Several prototypes with lower tolerance level for the channel dimensions were built where extensive and thorough cleaning process had been used but did not yield the expected result. Based on the previous experience, the design was reverted

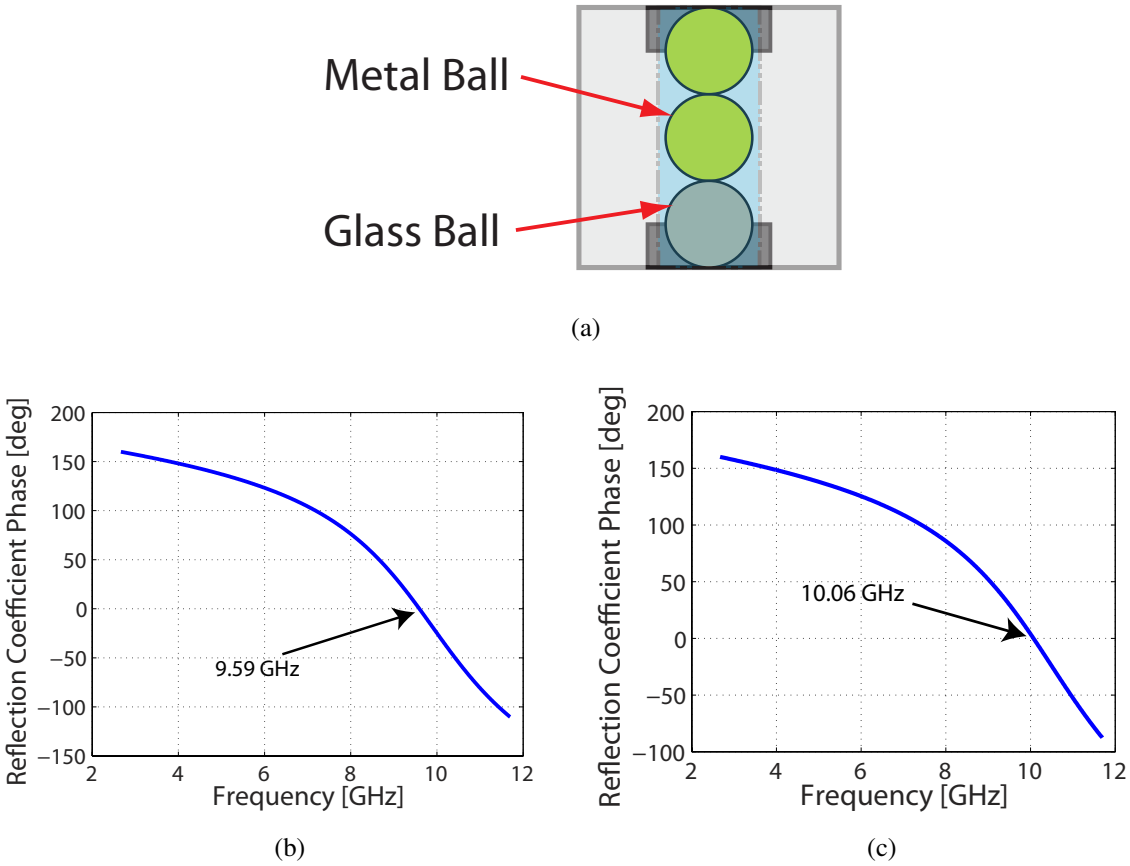

Figure 2.7: (a) Unit cell of one embodiment of the proposed tunable reactive impedance surface [Back View]. This structure has unit cell dimensions of 6 mm $\times$ 6 mm and uses three balls per unit cell to achieve tunability (b) Simulated phase response when the metal ball is underneath the gap and (c) Simulated phase response when the glass ball is underneath the gap of capacitive patches.

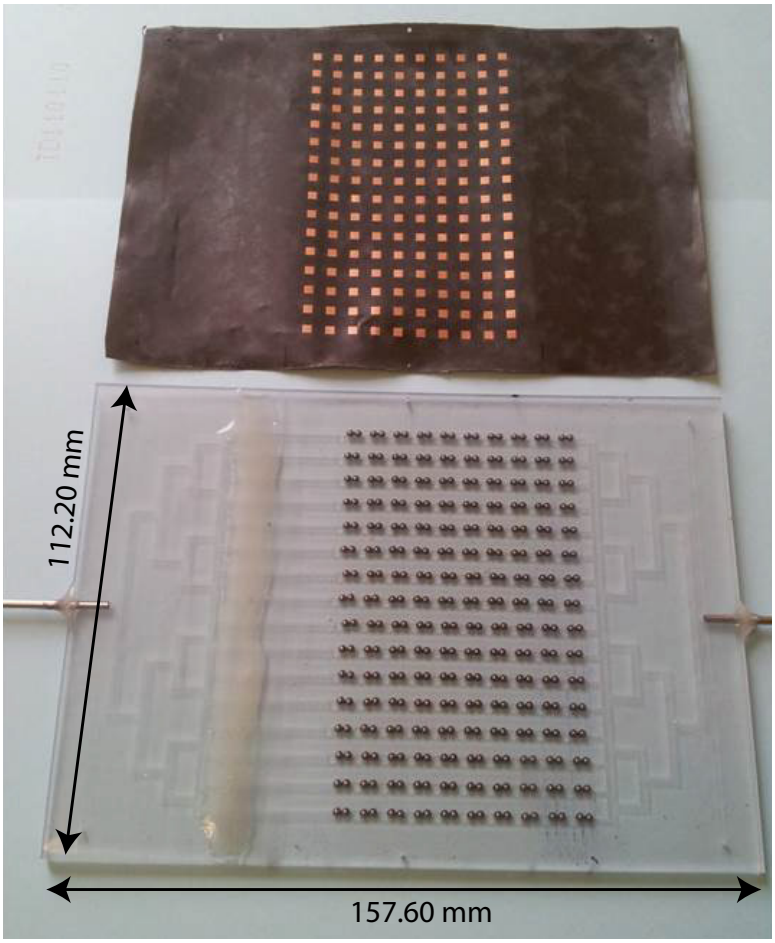

Figure 2.8: [Top] Photograph of the capacitive patch array fabricated on a 5 mils-thick Rogers 5880 laminate, [Bottom] 3D printed slab with 16 fluidic channels (structure with 6 mm unit cells).

back to the 8 channel prototype with channel cross-section of 2.2 mm $\times$ 2.2 mm. However, the number of channels were scaled up to 16. It is believed that by increasing the channel cross-section, any imperfection inside the channels would be negligible for the balls when in motion and minimal variation in pressure-drop occurring when fluid moves through different parts of the channels. In addition to that, cleaning the support structures from inside the channels would be relatively easy. Preliminary simulation of a unit cell of this structure was performed using CST Microwave Studio to evaluate its tuning capability. It was found out that a structure with

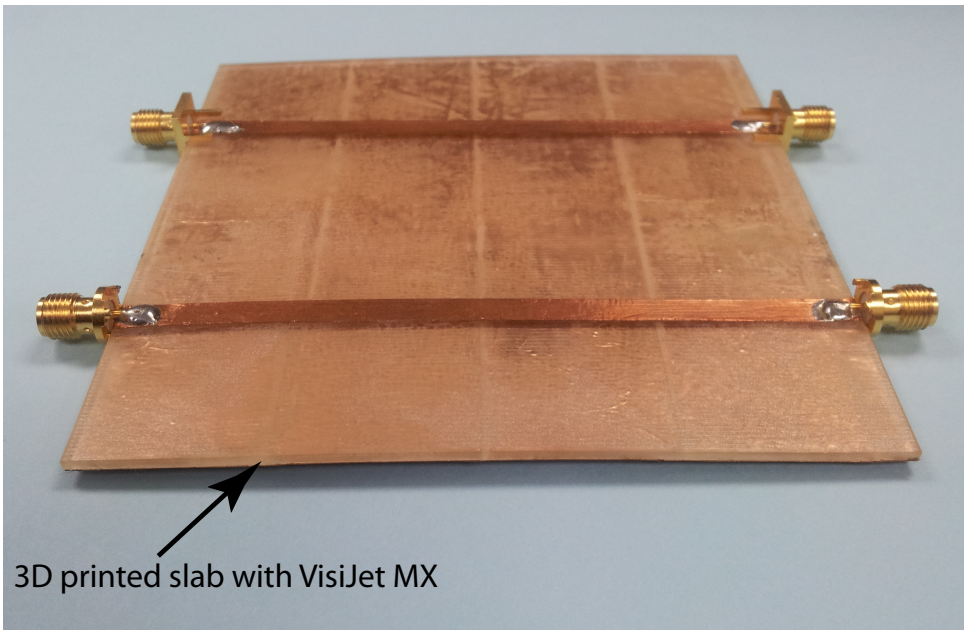

Figure 2.9: VisiJet MX dielectric characterization setup.

a unit cell size of 6.0 mm with an overall substrate thickness of 3.22 mm can provide 0.47 GHz of tuning range, a trade-off in terms of frequency tuning performance compared to the 7.0 mm unit cell structure. The 3D printed substrate thickness was chosen by taking into account the minimum dimensions of the channels that the 3D printer can accurately fabricate. The unit cell had 2 metal balls and 1 glass ball all with a diameter of 2.0 mm (see Fig. 2.7(a)). The metal balls are modeled as PEC and the glass ball is modeled as a dielectric with ϵ_r = 6.9. The gap between the two adjacent capacitive patches was 3.6 mm, which was determined based on the design guidelines mentioned in [39]. The position of each ball was moved one at a time and the phase of the reflection coefficient was recorded to evaluate the tuning range. The unit cell configuration of 2.7(a) gives the response shown in Fig. 2.7(b). As the balls move, the phase change occurs gradually and eventually provides the response shown in Fig. 2.7(c), when the glass ball is underneath the gap. Fig. 2.8 shows the photograph of the 3D printed dielectric substrate with 16 embedded fluidic channels. The printing material used to build the structure was Accura 60. Each ball was inserted into the channels one at a time by hand. The channels

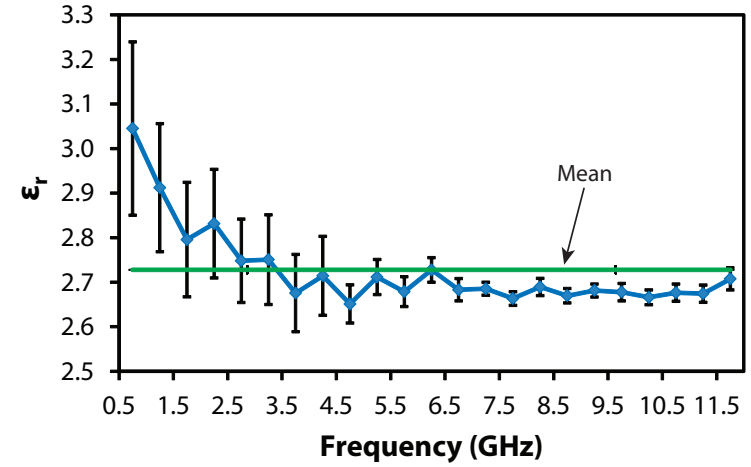

(a)

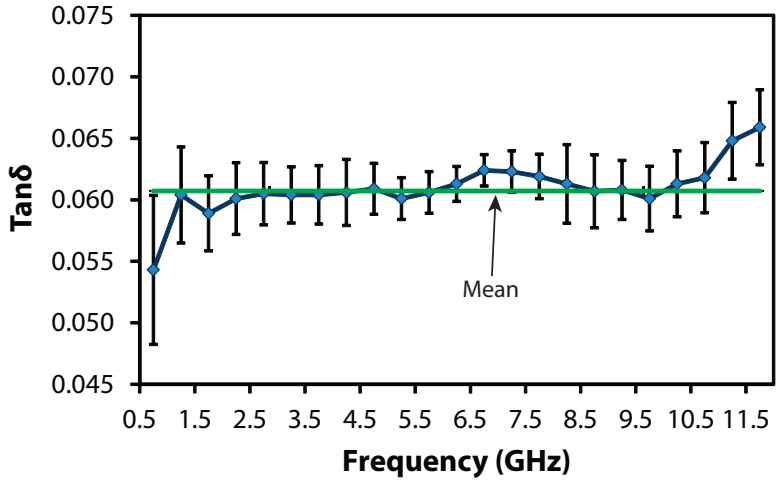

(b)

Figure 2.10: (a) Dielectric constant and (b) Loss tangent values of VisiJet MX material.

in the printed structure had a tolerance of 10% which was intentionally included in the design for easy clean up of the residues of support structures built by the printer during the printing process as well as for the easy movement of the balls inside the channels. Before covering one side of the printed slab with a ground plane and the other side with a periodic array of sub-wavelength capacitive patches, the outlets on two sides were sealed off with blunt needles. The inside of the channels were then filled with mineral oil using 10 ml syringes. As one of

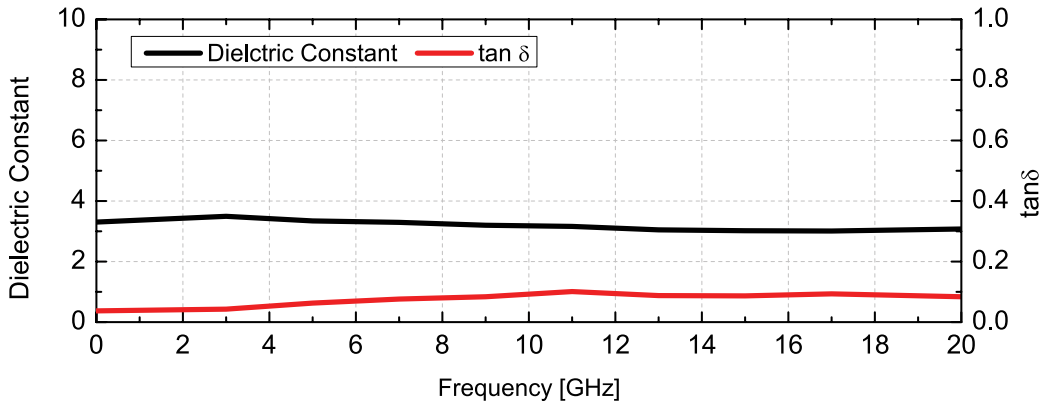

Figure 2.11: The dielectric constant and loss tangent values of Accura 60 material.

the syringes was pushed, synchronous movement of the trains of metal and glass balls was observed.

2.4 Measurement Results

Measurements were performed for the RIS in a laboratory setting. The dielectric constant and loss tangent of a slab of VisiJet MX were characterized in the lab using methods described in [54]. The process is as follows - a thin slab was printed and two separate transmission lines (see Fig. 2.9) were fabricated on the slab using copper tape. The S parameter was measured using only one transmission line with a vector network analyzer. The S parameter data was then loaded into Agilent ADS and the dielectric constant and loss tangent values were extracted. Ten separate tests were performed and finally the mean was taken to determine the dielectric constant and loss tangent values, which are 2.73 and 0.06 respectively, as shown in Fig. 2.10. The dielectric constant and loss tangent values of Accura 60 were also characterized using the methods described in [54] and the results are shown in Fig. 2.11. An X-band standard gain horn antenna was used to measure the reflection from the structure. The horn was placed approximately 68 mm away from the structures in a way so that the E-field of the radiated wave is parallel to the channels. As synchronization of the 7.0 mm unit cell structure was not achieved, the RIS was manually moved back and forth along the channels. The reflection

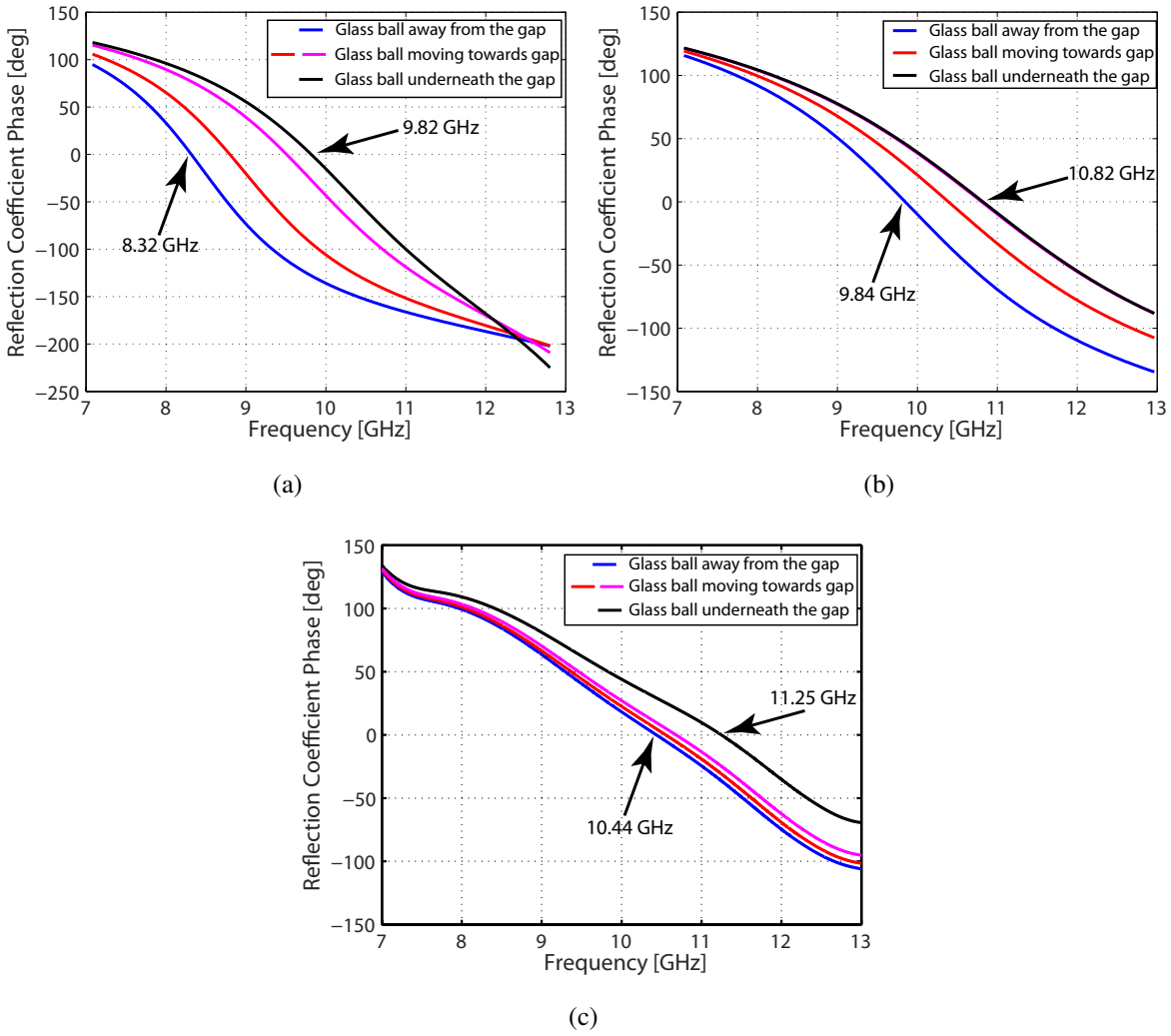

Figure 2.12: Tuning range of the 7.0 mm unit cell structure (a) Simulated [Balls are aligned] (b) Simulated [Balls are misaligned] and (b) Measured.

coefficient measurement was then performed using an Agilent N5225A PNA. Before placing the RIS on top of the 3D printed slab, a brass sheet with the same thickness and dimensions as those of the RIS was placed on top of the slab and the reflection coefficient was measured. The reflection coefficient phase from the brass sheet was later used to normalize the measured phase of the capacitively loaded periodic structure. Thus, the actual phase response of the structure was extracted. From the measurements, the maximum tuning range achieved was

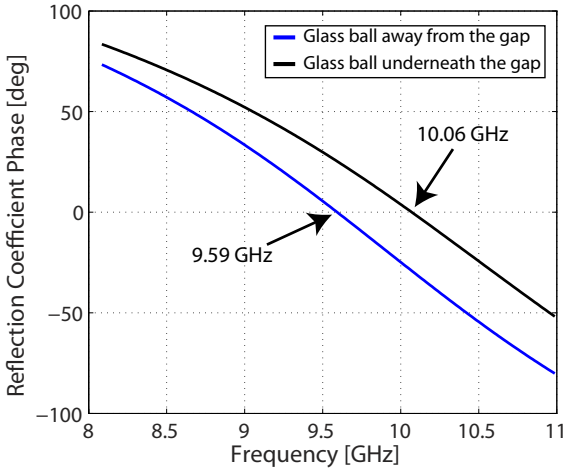

(a)

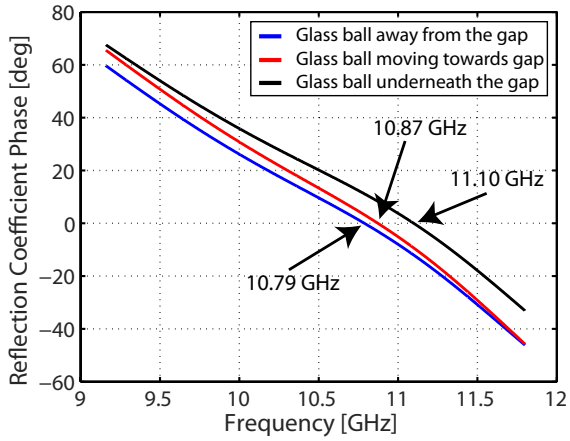

(b)

Figure 2.13: Tuning range of the 6.0 mm unit cell structure (a) Simulated and (b) Measured.

observed to be 0.81 GHz - as can be seen in Fig. 2.12(c). A rather significant deviation from the simulated response - shown in Fig. 2.12(a) is also observed. This is primarily attributed to the limited accuracy of the measurement technique used to characterize the dielectric constant and loss tangent values of VisiJet MX substrate (see [54]). Additionally, it was observed that the balls inside the channels were oriented in a slightly zigzag fashion due to space available from the tolerance incorporated into the channels during the design process. A simulation

was performed to see if the orientation of the balls inside the channels impacts the tuning range of the overall structure. It was observed that the tuning range actually dropped to 0.98 GHz, shown in Fig. 2.12(b). Moreover, because of the small thickness of the laminate used to fabricate the capacitive patch array on, isolated air gaps were observed to exist between the capacitive patch array and the 3D printed substrate. Since these air gaps were isolated and did not exist uniformly over the entire surface area of the RIS, they were not modeled in the simulations. For the 6.0 mm unit cell structure, the trains of balls were moved by slowly pushing one of the syringes attached to the slab through a blunt needle. After each small movement of the trains, the reflection coefficient measurement was performed using the same Agilent PNA. From these measurements, the maximum tuning range achieved was observed to be 0.31 GHz- as can be seen in Fig. 2.13(b). It should be noted that the frequency range of the reflection coefficient phase data is limited by the available bandwidth of the X-band horn. A rather significant deviation from the simulated response- shown in Fig. 2.13(a) is also observed. Therefore, the discrepancies between the measurement and simulation results can be attributed to the above-mentioned factors.

2.5 Conclusions

We presented a technique that is expected to enable the fluidic tuning of large-scale periodic structures with multiple unit cells. The proposed technique eliminates the use of liquid-metal filled capillary tubes by using a 3D printed dielectric slab with embedded channels and populated with metal and glass balls. A prototype with 8 parallel channels was fabricated and synchronous movement of periodic trains of metallic and glass balls in different channels was observed experimentally. Then an array of sub-wavelength capacitive patches was combined with a 16 channel prototype to obtain a tunable RIS and a frequency tuning range of $10.79 - 11.10$ GHz was experimentally demonstrated. The mechanical tuning speed of the structure is constrained by the 10 ml syringes, the inside surface roughness of the channels and them being free of residues. A 6 mm unit cell of the structure with a 2 mm diameter channel results in 18.84 μl. Based on the availability of various commercial micropumps, the tuning speed can

vary between several micro-seconds to few milli-seconds. During this process a 16 channel prototype consisting of 7.0 mm unit cells is built with smaller channel cross sections. It has been observed that synchronization of ball movement is difficult to obtain due to manufacturing limitations associated with 3D printing. However, based on simulations performed, the structure is observed to be capable of giving 1.5 GHz of tuning range and from measurement a 0.81 GHz of tuning range has been achieved. Additional simulation has shown that a structure consisting of 8.8 mm unit cells and 0.8 mm diameter balls can provide 2.14 GHz of tuning range.

Chapter 3

A Fluidically-Tunable, Dual-Band Patch Antenna With Closely-Spaced Bands of Operation

3.1 Introduction

With the recent developments in wireless communication and voracious appetite for data, there is a growing trend towards using wireless devices that operate at two or more frequency bands. The frequency bands used for a given wireless application (e.g. cellular communication) generally vary based on the geographical location and the service provider. This has been a motivating factor for developing antennas that can work at multiple bands simultaneously and dynamically change their operating bands that they work at if needed. Reconfigurable antennas in the past decade or so have gained a remarkable research interest. They are used to support multiple telecommunications standards, to mitigate strong interference signals, or to cope with a changing environment [55] - [56]. Using reconfigurable antennas can also enable the efficient use of power and spectrum, reduce the number of complex hardware, and potentially reduce the cost of the system.

Reconfigurable antennas may be designed to provide tunable frequency bands, dynamically alter their polarizations, or have variable radiation patterns. Various techniques have been used to achieve agility in frequency, polarization and beam direction of antennas. Among these, using radio-frequency microelectromechanical systems (RF-MEMS), variable capacitors (varactors), PIN diodes, photoconductive elements, physical alteration of the radiating structure, and advanced materials such as ferrites and liquid crystals can be mentioned [10], [55] - [61]. For example, in [57], PIN diode switchable slots are used in a microstrip patch antenna to

achieve circular polarization diversity. In [60], a rectangular spiral antenna is loaded with a set of MEMS switches to provide scan-beam capability and in [61] a varactor-tunable, dual-band slot antenna is presented. While there are many more examples of reconfigurable antennas available in the literature, these examples sufficiently illustrate the variety of different electronic techniques used to reconfigure the various properties of antennas. Electronically-tunable antennas, however, suffer from nonlinearities under moderate to high peak-power excitation levels. These nonlinearities can result in intermodulation distortion and RF-induced changes of the antenna's radiation parameters . This limits the use of these tuning techniques mainly to the receiving systems or low-power transceivers.

In this chapter, we present a new concept for designing dual-band patch antennas with closely-spaced bands of operation and similar radiation characteristics at both bands. This technique can be used to design dual-band antennas with frequency ratios as low as f_2/f_1=1.08. We also present a fluidic technique that can be used to dynamically tune the frequency responses of the proposed antenna. The fluidic tuning technique used in this work is similar to those used to design tunable periodic structures in [39], [62]. In [39], these techniques were demonstrated to be far superior to electronic tuning technique in terms of the linearity of the response of the structure when subjected to moderately high-power levels (10s of Watts). A prototype of this dual-band tunable antenna is designed and fabricated, and experimentally characterized in the lab. The results presented in this chapter are significant for two reasons. First, designing dual-band antennas with small band separation, and similar radiation characteristics at both bands, is a rather challenging task. Therefore, the concept presented in this work (even in its static form) is expected to find applications in practical systems that need to operate under such conditions. Secondly, the proposed mechanical tuning technique is ideally suited for transceiver systems that need to work with moderate to high peak power levels. This is an area where most conventional electronic tuning techniques drastically underperform.

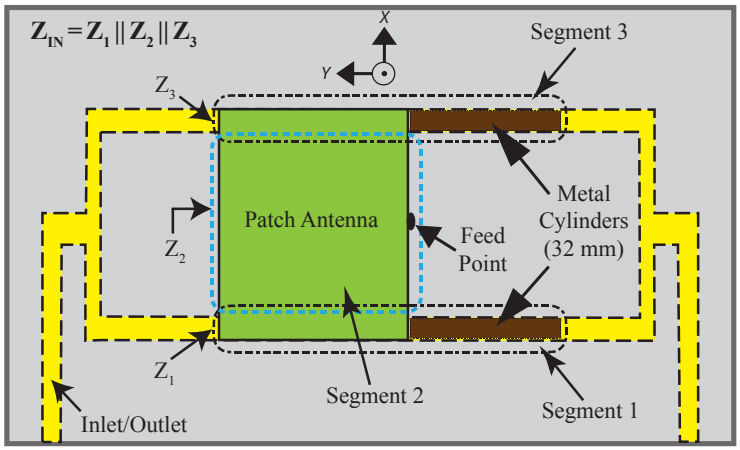

(a)

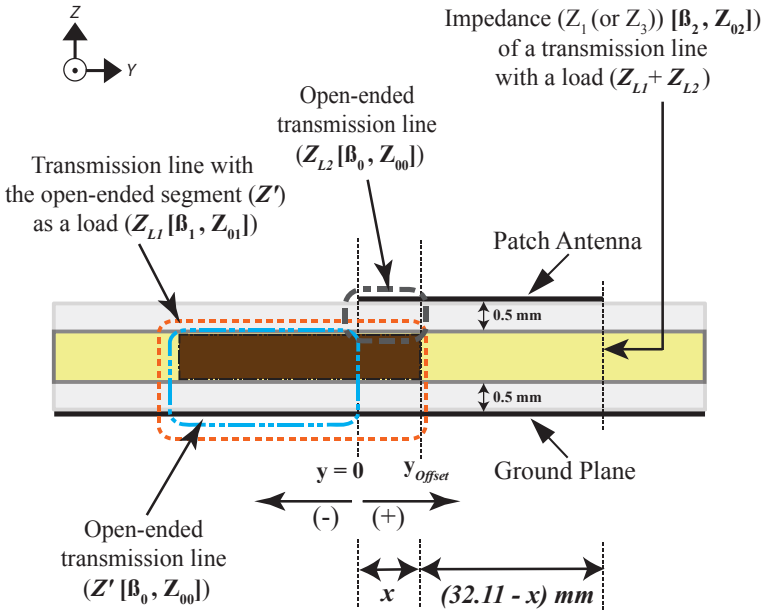

(b)

Figure 3.1: Layout of the fluidically-tunable, dual-band patch antenna. (a) Top view. (b) Side view.

3.2 Principles of Operation and Design Procedure

Fig. 3.1 shows the topology of the proposed antenna. Two 2.0 mm diameter channels, filled with mineral oil ($\epsilon_r \approx 2.15$, measured with an Agilent 85070E Dielectric Probe Kit), are

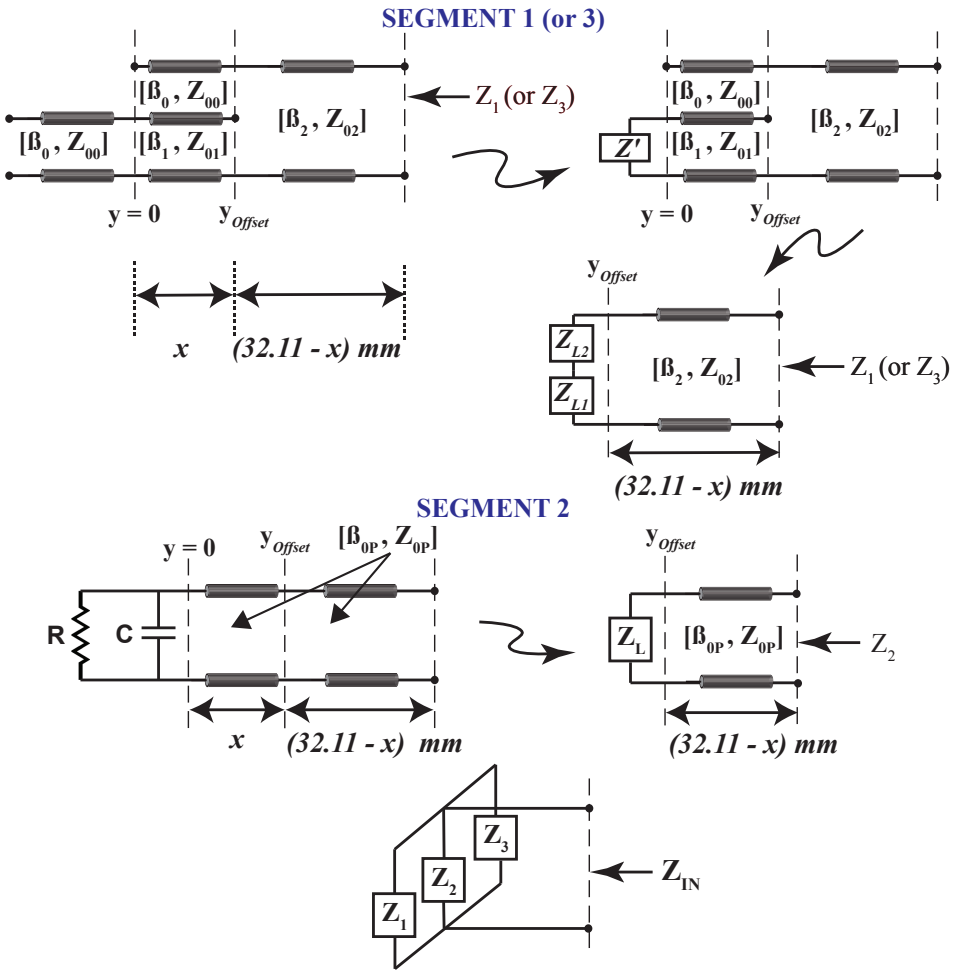

Figure 3.2: Transmission-line based equivalent circuit model of the proposed antenna.

located under the non-radiating edges of the patch. In each channel, a metallic cylinder with a length of 32 mm is located that can be moved when the liquid within the channels move. The metal cylinders move along the y axis from right to left (Fig. 3.1(a)). The channels are connected to the inlet and outlet using a symmetric pressure distribution network that ensures the movement of the cylinders within each channel is synchronized (see [62]). The patch operates at around 2.5 GHz without any metal cylinders underneath it. As soon as the cylinders come close to the patch, i.e. when $y_{offset} \approx 0.0$ mm, the main resonance of the patch splits into two resonances and the separation increases with increasing y_{offset}. To understand the

dual-band behavior of the antenna, a simple model of the antenna was developed and analyzed. The patch antenna was divided into three segments as shown in Fig. 3.1(a) with dimensions of 2 mm $\times$ 32.11 mm for segments 1 and 3, and dimensions of 37.4 mm $\times$ 32.11 mm for segment 2. The impedances, Z_1, Z_2 and Z_3, at the left radiating edge are determined and the total input impedance of the antenna is then calculated. In Fig. 3.1(b) and Fig. 3.2, a detailed breakdown for segment 1 (or 3) is shown. The left portion of the cylinder from the y = 0 marker is modeled as an open-ended transmission line with wave propagation constant of β_0 and characteristic impedance of Z_{00}. The area between the cylinder and the ground plane, between y = 0 and y_{offset}, is modeled as another piece of transmission line with β_1

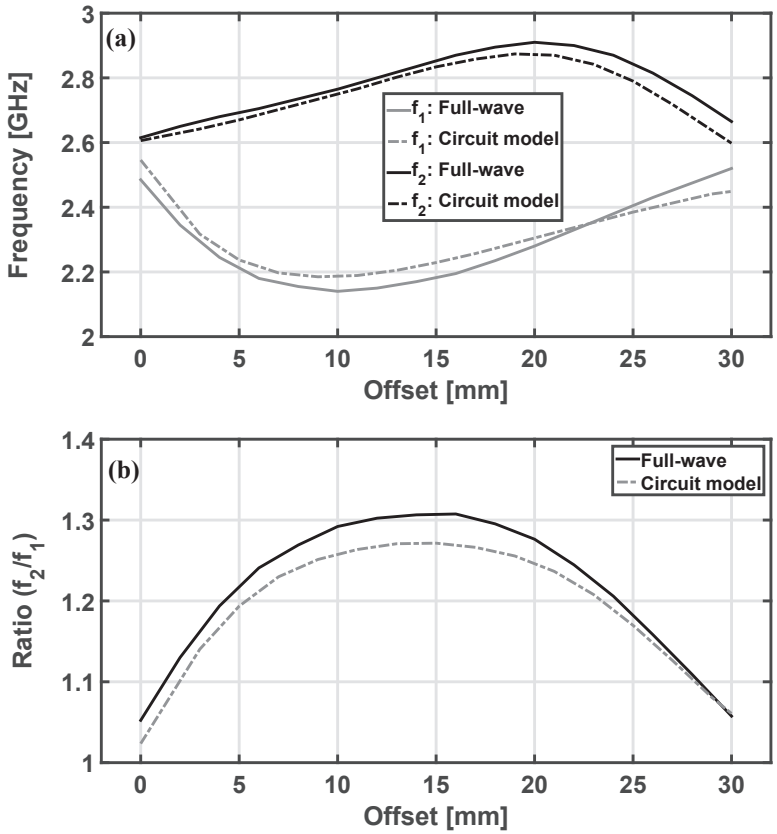

Figure 3.3: (a) Variations of the two resonant frequencies. (b) Ratio of the frequencies, f_2/f_1, as a function of y_{offset}.

and Z_{01} terminated at a load of Z'. The area between the cylinder and the patch antenna, between $y = 0$ and y_{offset}, is modeled as another open-ended transmission line with the similar wave propagation constant and characteristic impedance of Z'. The right section from the y_{offset} marker is modeled as a transmission line with β_2 and Z_{02} with the series combination of Z_{L1} and Z_{L2} as its load. The relative dielectric constant for segments 1 and 2 are extracted

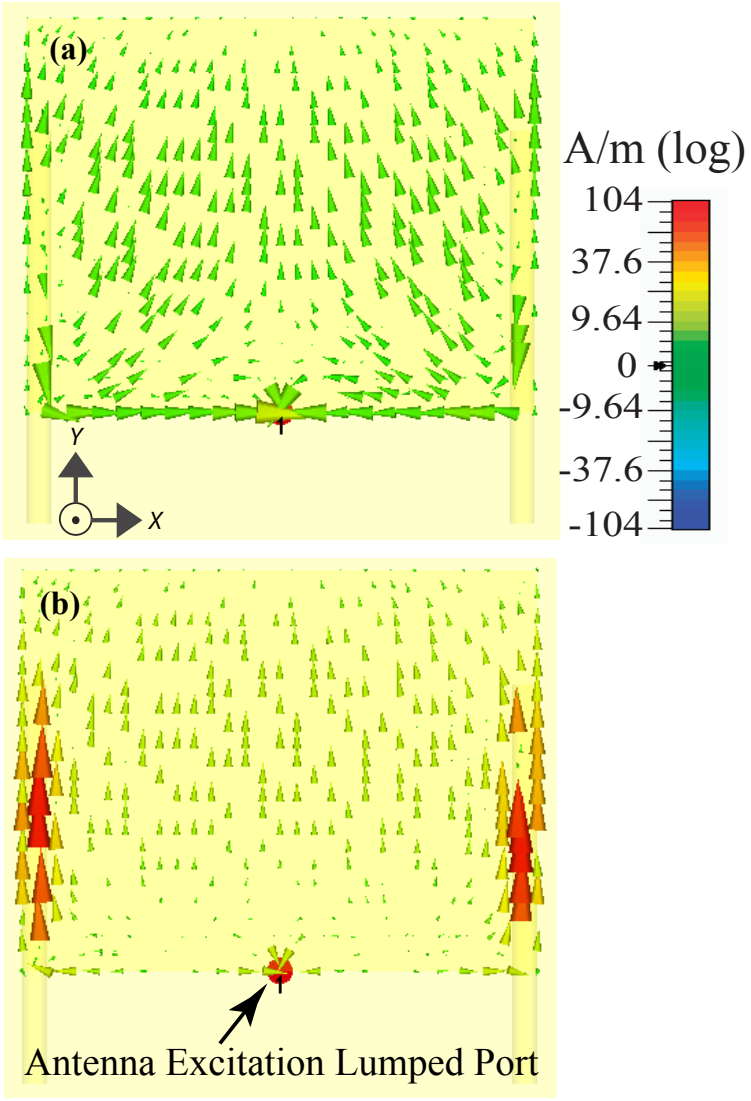

Figure 3.4: Simulated electric current distribution on the patch surface for y_{offset} = 23 mm. (a) At f_1 = 2.36 GHz. (b) At f_2 = 2.89 GHz.

using CST Microwave Studio and Agilent ADS to compute wave propagation constant (β) values. The characteristic impedances of these transmission line segments are calculated using formulas available in literature to compute characteristic impedance of a microstrip line. The impedance of segment 2 in Fig. 3.1(a) is calculated using formulas (for transmission line model of patch antenna) available in [63]. The total impedance, Z_{IN}, looking from the left radiating edge is the parallel combination of impedances Z_1, Z_2 and Z_3 (see Fig. 3.2). Fig. 3.3(a) shows the variation of the first and and second resonant frequencies of the antenna as a function of the offset distance, y_{offset}, from both full-wave simulations and the proposed analytical model. As can be observed, as y_{offset} increases, the frequency of the first (second) resonance, f_1 (f_2) decreases (increases) first. Subsequently, as y_{offset} increases further, this trend is reversed. From the simulations (circuit model), the ratio of the frequencies f_2/f_1 changes from 1.05 (1.02) to 1.31 (1.27) as a function of the offset distance. Fig. 3.4 shows the electric current

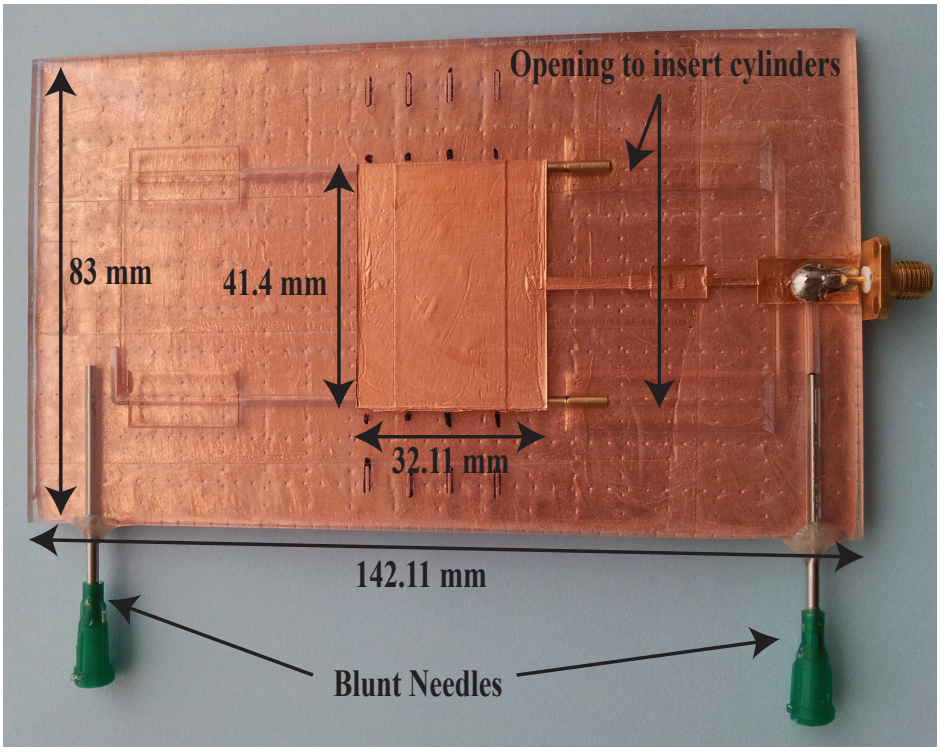

Figure 3.5: Photograph of the fabricated prototype with two visible brass cylinders.

distribution on the surface of the antenna at the two resonances. Careful examination of these currents reveals that they will result in similar radiation characteristics (polarization, radiation pattern shape, and the direction of maximum radiation) in the far field. Therefore, this dual-band antenna is expected to provide similar radiation characteristics at both of its bands of operation.

The patch antenna is designed to operate at 2.5 GHz. Accura 60, a type of photopolymer resin that is 3D printed, is used as the substrate of the antenna. The substrate is 3.35 mm thick and has a dielectric constant of 3.2 and a loss tangent of 0.05 [62], which is included in the simulations. Note that this material was used solely because it was readily available for our use in this proof-of-concept demonstration. However, for a system-level application it is recommended to use 3D printed materials with lower loss values. The patch antenna has dimensions of 41.4 mm $\times$ 32.11 mm. In the initial simulations, the antenna was fed with a lumped port placed at the edge of the radiating slot (see Fig. 3.4(b)). This is done to calculate the input impedance of the antenna at the edge of the radiating slot. The value of

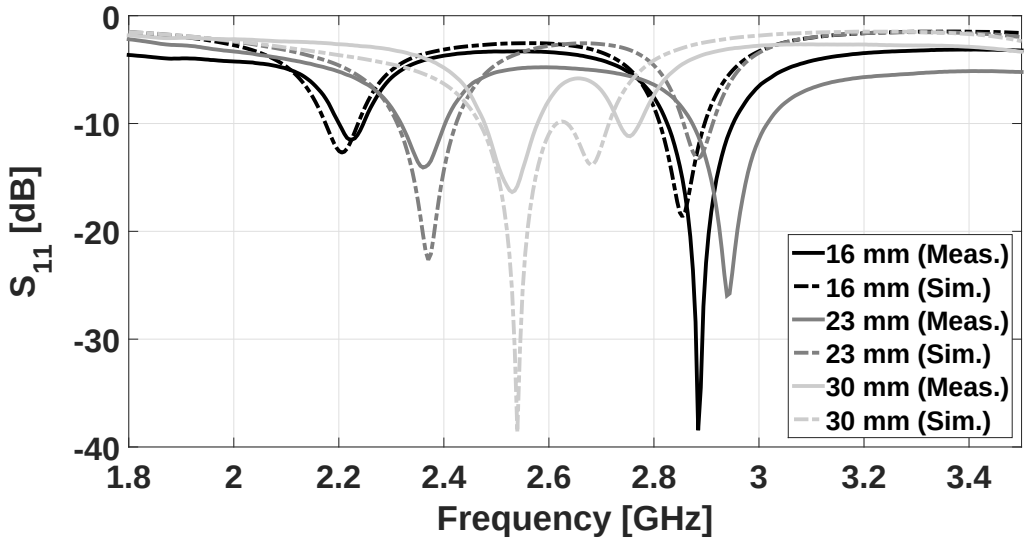

Figure 3.6: Simulated and measured input reflection coefficients of the patch antenna for y_{offset} = 16 mm, y_{offset} = 23 mm, and y_{offset} = 30 mm.

this input impedance was subsequently used in the impedance matching process. The response of the antenna was simulated using CST Microwave Studio. The patch and metal cylinders were modeled as copper and brass respectively in the simulations. The substrate length is approximately four and a half times of the length of the patch and the width is twice of the patch width. The length of the substrate was chosen to be 4.5 times the patch length so that there was enough space for the metal cylinders to rest without coming in close proximity to the patch and also accommodate the inlet/outlet channels.

3.3 Prototype Fabrication and Measurement Results

The substrate of the proposed antenna was fabricated using a Dimension Elite 3D printer and is shown in Fig. 3.5 (notice that the substrate is transparent). An impedance matching network consisting of a series of transmission lines was designed to ensure proper matching for all values of y_{offset}. The patch antenna along with the matching network was assembled on top of the substrate with copper tape (see Fig. 3.5). Two 32 mm long brass cylinders with diameter 2.0 mm were inserted into the channels. The openings were later covered with 3D printed pieces and sealed off with epoxy. The channels were filled with mineral oil using a 10 ml syringe through one of the inlets/outlets. After the channels were filled up, the other inlet/outlet was mounted with a partially oil-filled 10 ml syringe. One of the syringes was pressed to move the cylinders together along the channels and position them at a specific y_{offset}. The S_{11} of the antenna was then measured using an Agilent N5225A PNA for three different offsets, y_{offset} = 16 mm, y_{offset} = 23 mm and y_{offset} = 30 mm. The results are shown in Fig. 3.6. It can be seen from the results that there are discrepancies between measurements and simulations in the form of frequency shift and lower/higher reflection coefficient values at the resonant frequencies. These can be attributed to several factors such as imperfections arising in the dimensions of the patch antenna and/or matching network due to the use of copper tape and limited accuracy of measurement technique used to characterize dielectric constant and loss tangent values of Accura 60 substrate (see [54]).

Table 3.1: Total efficiency and peak directivity of the antenna at the resonant frequencies for y_{offset} = 16 mm, 23 mm, and 30 mm.

	Simulation		**Measurement**	
Frequency [GHz]	2.2	2.85	2.22	2.88
Total Efficiency	28%	29%	27%	31%
Peak Directivity (dBi)	6.38	6.89	6.97	6.36
Frequency [GHz]	2.37	2.88	2.35	2.93
Total Efficiency	33%	22%	32%	25%
Peak Directivity (dBi)	7.15	6.69	7.27	6.49
Frequency [GHz]	2.54	2.68	2.53	2.74
Total Efficiency	34%	21%	38%	18%
Peak Directivity (dBi)	7.34	6.3	7.11	8.11

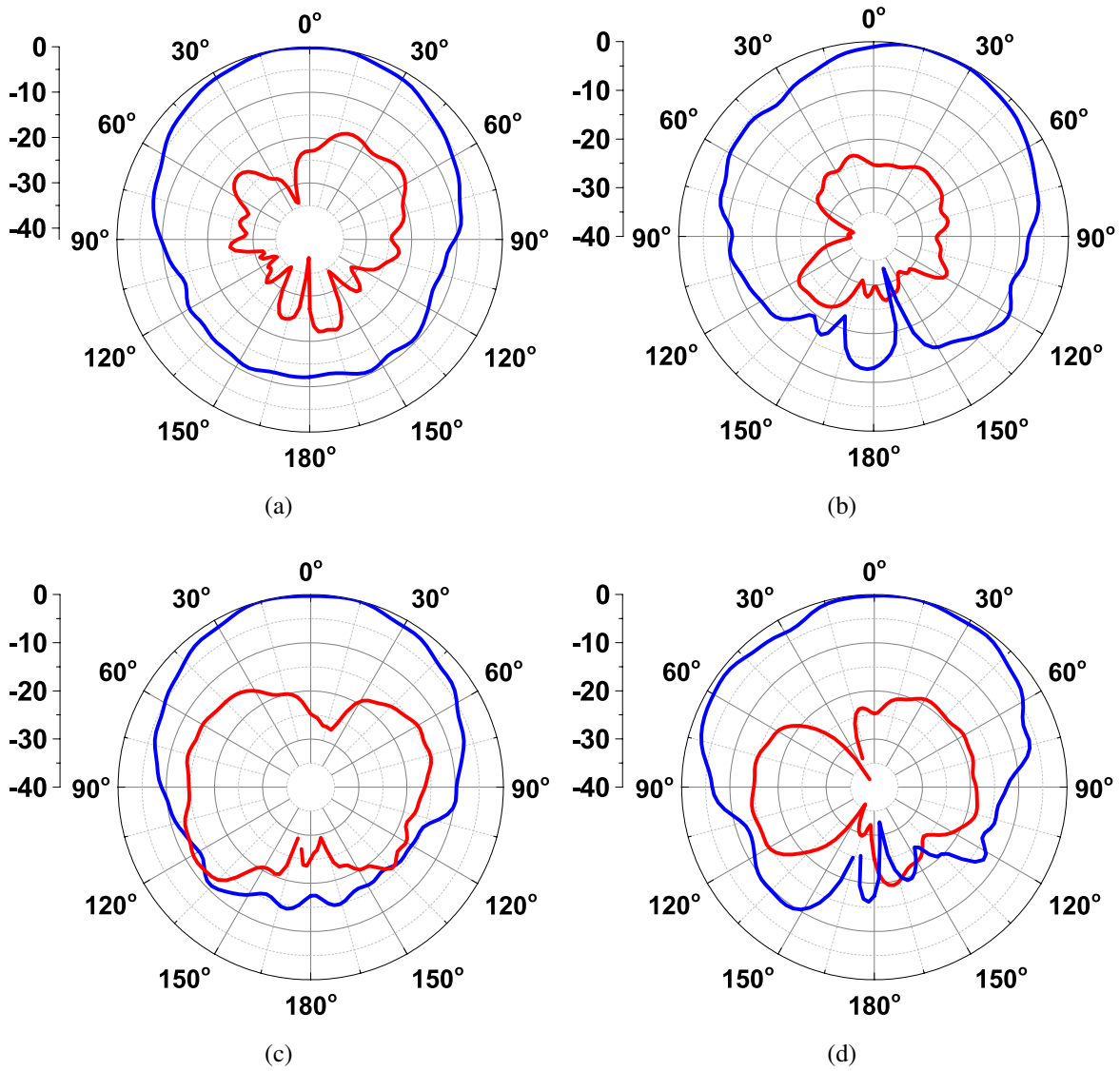

Figure 3.7: Measured normalized gain patterns of the antenna. (a)-(d) Radiation patterns [co-pol (blue) and cross-pol (red)] at 2.35 GHz and 2.93 GHz when y_{offset} = 23 mm. (a) H-plane at 2.35 GHz (Max. Gain = 1.48dBi). (b) E-plane at 2.35 GHz (Max. Gain = 2.31dBi). (c) H-plane at 2.93 GHz (Max. Gain = 0.45dBi). (d) E-plane at 2.93 GHz (Max. Gain = 0.41dBi).

The radiation patterns of the antenna were measured using a multi-probe near-field antenna measurement system (Satimo StarLab). Measurements were done for y_{offset} = 16 mm, 23

mm, and 30 mm respectively. Fig. 3.7 shows the co- and cross-pol radiation patterns when y_{offset} was 23 mm. The tilt observed in the E-plane pattern is attributed to the presence of the cylinders, the feed network and relatively long feeding cables along the E-plane. Table 3.1 compares the simulated and measured total efficiencies as well as the peak directivity of the antenna for three y_{offset} values. The relatively small total efficiencies are primarily attributed to the high losses of the 3D printed dielectric substrate. This, however, is not an inherent limitation of the proposed design. The radiation efficiency of the antenna can be significantly enhanced if lower loss materials are used to implement the substrate. The mechanical tuning speed of the structure is constrained by the 10 ml syringes, the inside surface roughness of the channels, and them being free of any residues that remain from the fabrication process. Based on the availability of various commercial micropumps, the tuning speed of antennas of this type is expected to vary between 100s of micro-seconds to hundreds of milli-seconds.

3.4 Conclusions

The design and principles of operation of a new type of dual-band patch antenna with closely-spaced bands of operation were presented and discussed. It was also demonstrated that the response of this antenna can be made tunable using a fluidic tuning technique. A simple transmission-line-based equivalent circuit model was also developed to predict the behavior of the two resonances of the antenna when it is tuned using the proposed fluidically tuning mechanism. The frequency variation trend predicted by the model closely matches the trend extracted from the full-wave simulations. A prototype was also fabricated and characterized. Measurement results show a return loss better than 10 dB and consistent, similar radiation patterns at both bands of operation across its entire frequency band of operation. In the specific example discussed in this chapter, a frequency ratio of f_2/f_1 = 1.08 - 1.30 was achieved from measurement. The radiation efficiency of this antenna can be enhanced dramatically if a lower loss dielectric substrate is used. This antenna is expected to be useful both in its static mode of operation (i.e. non-tunable) in conventional dual-band systems and its tunable version in

systems that need to transmit signals with high (10s of Watts) peak power while maintaining linearity.

Chapter 4

Fluidically-Steerable 3-Element Parasitic Patch Antenna Array

4.1 Introduction

Phased array antennas are widely used in various civilian as well as military applications. They can be broadly divided into two categories - Active Electronically Steerable Array (AESA) and Passive Electronically Steerable Array (PESA). In a PESA configuration, a single microwave source feeds the array elements via a corporate feed network within which variable phase shifters are integrated. On the other hand, in an AESA configuration, each element of the array is fed by a transmit/receive (T/R) module which consists of power amplifier, phase shifters, low-noise amplifiers and other components of a fully developed transceiver. Due to the expensive nature of the T/R modules, it is not economically feasible for widespread use of phased array antennas. Therefore, significant research interest has been generated not only in developing economically viable T/R modules but also coming up with innovative approaches to build phase array antennas without the use of phase shifters and/or T/R modules.

In a switched parasitic antenna, the direction of the radiation pattern can be controlled by electronically changing the characteristics of nearby parasitic elements close to the driven element [50]. Electronically steerable parasitic array radiators (ESPARs) are closely related to switched parasitic antennas [10], [64]- [68]. In ESPARs, passive elements are excited through mutual coupling between adjacent elements, which are also loaded with tunable reactive loads. Varying the reactive loads of each parasitic element changes the apparent magnitude and phase of the excitation of each element, which results in changing the direction of the beam towards

a desired direction [10]. ESPARs can provide a continuous change of the beam direction by using electronically-tunable elements. The vast majority of the ESPARs reported in the literature use electronic components such as solid-state or MEMS varactors [64]- [68]. Recently, an electronically steerable microstrip patch radiator has been presented in which varactors are loaded between the center driven element and the parasitic elements to control the mutual coupling [51]. Beside this, varactors are also loaded across the non-radiating edges of the parasitic elements to maintain resonance at the operation frequency and also uses aperture coupled feeding technique. The proposed design exhibits only a $\pm 15^{\circ}$ continuous scanning range but has better than 10 dB return loss value, no sidelobes and consistent half-power beamwidth compared to the boresight across the scanning range. This example sufficiently illustrates the nature of work found in the literature related to switched parasitic type antennas. However,

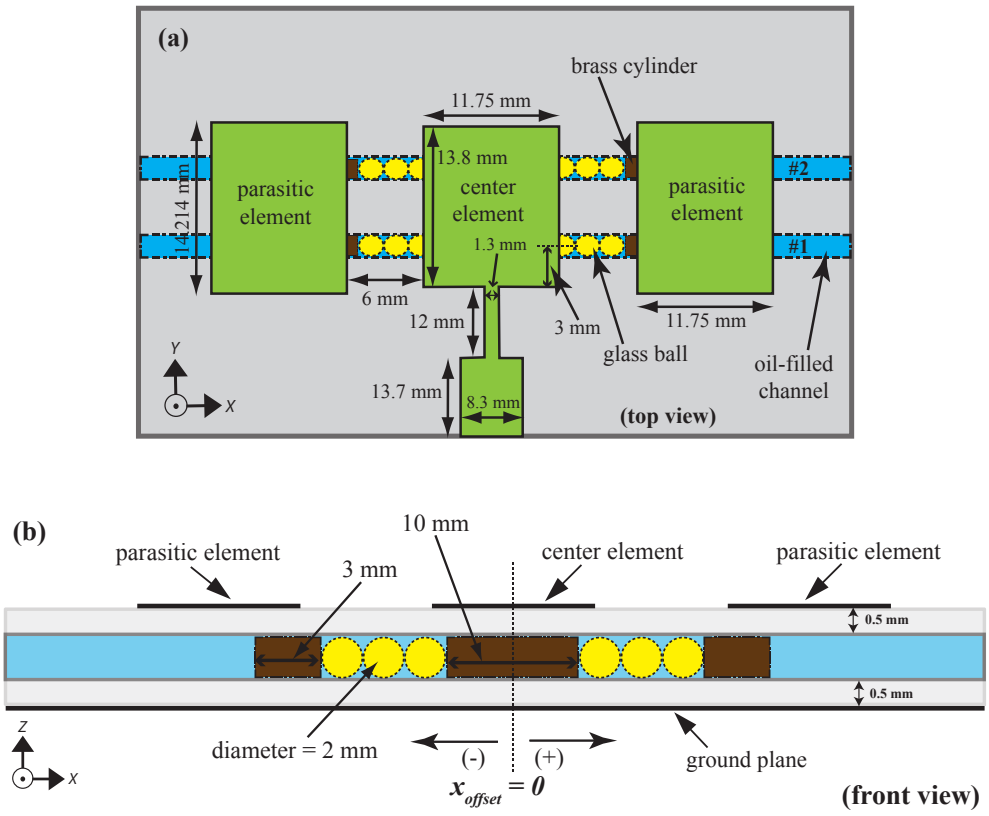

Figure 4.1: Layout of the mutually coupled proposed parasitic patch array.

electronically-tunable beam steerable antennas suffer from nonlinearities under moderate to high peak-power excitation levels. These nonlinearities can result in intermodulation distortion and RF-induced changes of the antenna's radiation parameters. This limits the use of these tuning techniques mainly to the receiving systems or low-power transceivers.

In this chapter, we present a new technique for designing a parasitic patch array whose beam direction can be steered using a fluidic tuning technique. The technique used in this work is similar to those used in designing tunable periodic structures as well as a dual-band patch antenna [39]- [62]. In [39], these techniques were demonstrated to be far superior to electronic tuning technique in terms of the linearity of the response of the structure when subjected to moderately high-power levels (10s of Watts). A prototype of the proposed beam-steerable antenna is designed, fabricated, and experimentally characterized. The fabricated prototype is composed of a main patch antenna element that is coupled to two adjacent parasitic patches and can provide a beam steering in the $\pm$ 22.5° range.

4.2 Design Procedure and Simulation

Fig. 4.1 shows the topology of the proposed antenna. The substrate of the antenna has dimensions of 70.5 mm $\times$ 60.2 mm. Two 2.0 mm diameter channels (numbered as 1 and 2),

Table 4.1: Summary of beam steering angles at the center frequency, 5.04 GHz, of simulated frequency band, 4.89 GHz - 5.21 GHz.

States	Channel 1 x_{offset} (mm)	Channel 2 x_{offset} (mm)	Scan Angle (deg.)
1	0	0	0
2	7.88	0	7
3	8.88	4.88	15
4	8.88	8.88	20

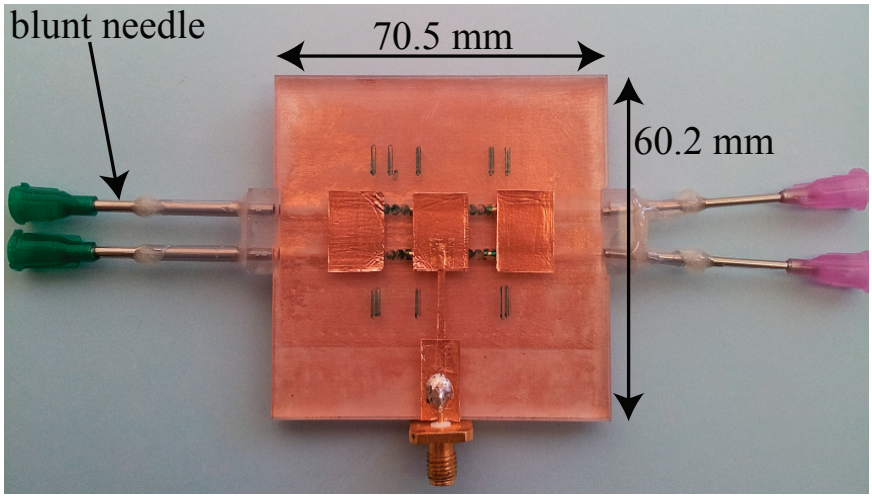

Figure 4.2: Photograph of a fabricated prototype.

filled with mineral oil ($\epsilon_r \approx 2.15$), are located under the radiating edges of the center and the parasitic patches. The centers of both channels are 3 mm apart from the radiating edges of the center element. A train of metal cylinders and glass balls are placed inside both channels as shown in Fig. 4.1. When x_{offset} = 0 mm (see Fig. 4.1(b)), the beam points to the boresight [$+z$ direction]. The beam is then steered depending on the direction of the movement of the cylinder and ball trains. For example, if the trains move towards the left of the x_{offset}= 0 marker ($-x$ direction), the beam is steered towards the opposite direction, i.e. $+x$ direction and vice versa (see Fig. 4.1). The appropriate placement of the trains along the channels causes the beam to be steered at a specific direction. When x_{offset} (corresponding to channel 1) is 7.875 mm, the beam is steered at 7° off broadside towards the $+x$ direction. As the beam is steered, the frequency response of the antenna is also affected. The placement of the trains in both channels that causes the beam to steer at various angles is summarized in Table 4.1. Extensive studies have been done to understand the effect of mutual coupling, impedance and current response in mutually coupled and reactance loaded parasitic array radiator [51], [69]- [70] and therefore has not been repeated here.

Preliminary simulations for this antenna are done in CST Microwave Studio. The placement of the channels, lengths of the metal cylinders, appropriate placement of the trains inside

the channels, dimensions of the center and parasitic patch elements have been optimized to achieve the beam steering angles shown in Table 4.1. An impedance matching network consisting of series transmission lines is developed to ensure proper matching for all the 4 states. Simulated S_{11} of the antenna is shown in Fig. 4.3 and the radiation patterns for states 1, 3 and 4 are shown in Fig. 4.4.

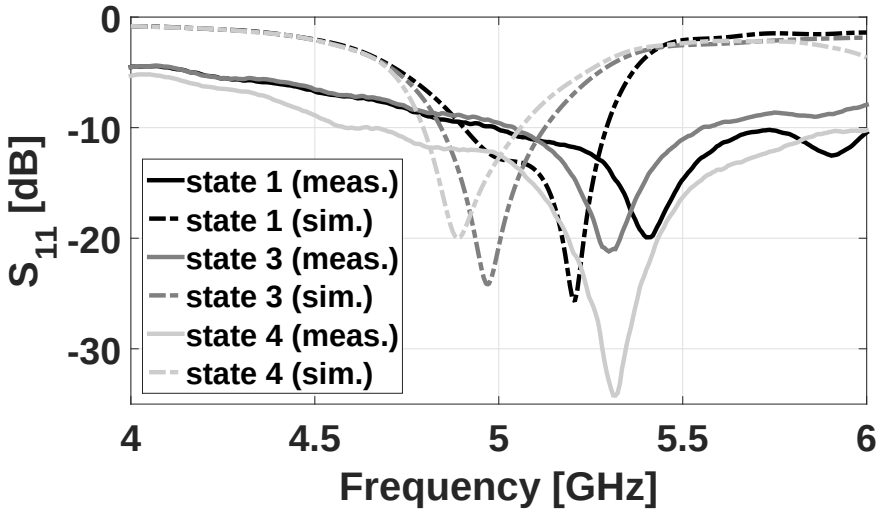

Figure 4.3: Simulated and measured input reflection coefficients of the antenna.

Table 4.2: Simulated and measured total efficiency of the antenna at 5.04 GHz and 5.35 GHz respectively for various states.

States	Total Efficiency	
	Simulation	*Measurement*
1	58.29%	51.50%
2	59.25%	”Not Measured”
3	60.52%	59.87%
4	55.97%	67.75%

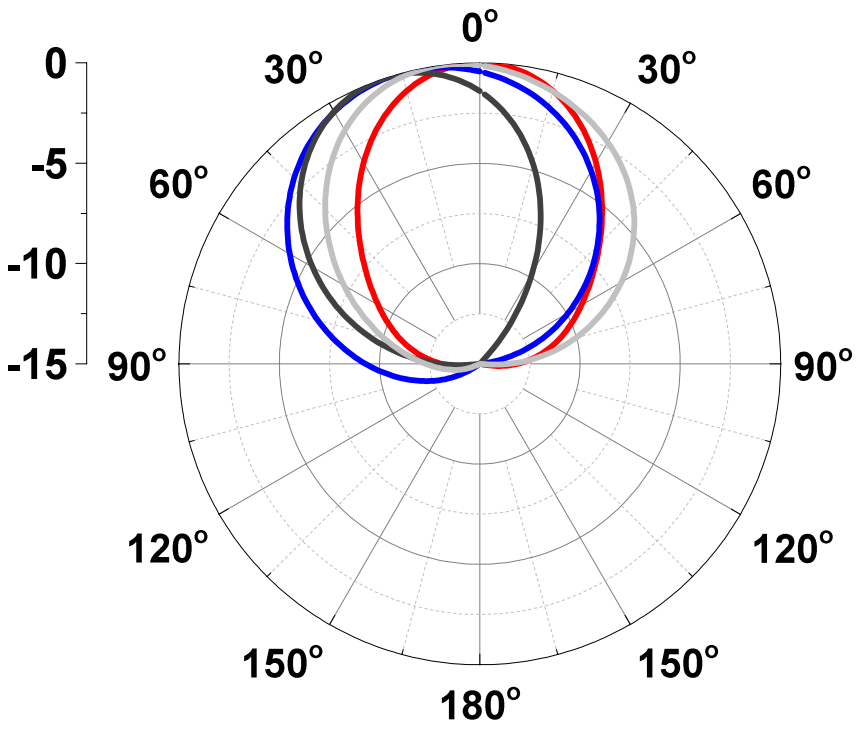

Figure 4.4: Simulated normalized H-plane gain patterns of the antenna. [Red] State 1 (Max Gain= 6.61 dBi). [Light Gray] State 2 (Max Gain = 5.844 dBi). [Blue] State 3 (Max Gain= 6.01 dBi) and [Dark Gray] State 4 (Max Gain= 6.78 dBi).

4.3 Fabrication and Measurement Results

The parasitic patch antenna array was designed to operate around 5 GHz. The substrate of the prototype was fabricated using a Dimension Elite 3D printer. The overall thickness of the substrate was 3.35 mm and was built with Accura 60, a type of photopolymer resin. The substrate has a dielectric constant of 3.2 and a loss tangent of 0.05 [62]. The patches were fabricated with copper tape on the top surface of the substrate. The channels were loaded with blunt needles and sealed off after they were populated with metal cylinders (brass) and glass balls as shown in Fig. 4.2. The channels are then filled with mineral oil using 10 ml syringes. By pushing the syringes separately, the metal cylinders and glass balls are positioned at the

appropriate locations corresponding to Table 4.1. The reflection coefficients were measured using Agilent N5225A PNA for the 1st, 3rd and 4th states shown in Table 4.1.

The radiation patterns of the antenna array were measured using a multi-probe near field antenna system (Satimo StarLab) at the center frequency, 5.35 GHz, of the measured frequency band (5.3 GHz - 5.4 GHz) for the three states (see Fig. 4.3). It can be seen from Fig. 4.3 that there are discrepancies between measured and simulated reflection coefficient values. These discrepancies can be attributed to several factors such as inclusion of tolerance in the final design of the substrate to ensure smooth movement of the cylinders and glass balls inside the channels, imperfections arising in the dimensions of the patches, metal cylinders, glass balls and/or matching network and limited accuracy of measurement technique used to characterize

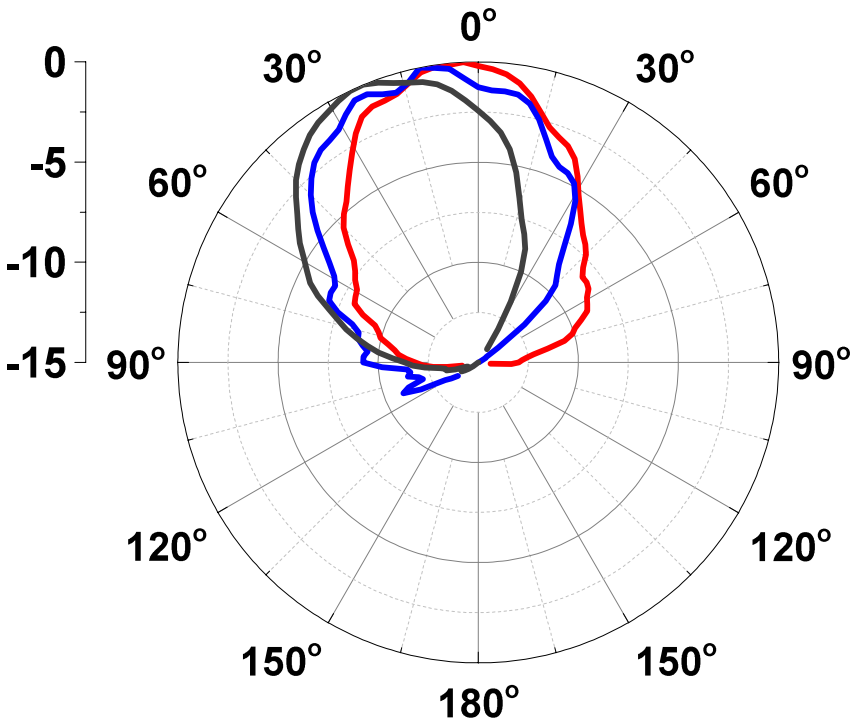

Figure 4.5: Measured normalized H-plane gain patterns of the antenna. [Red] State 1 (Max Gain= 4.47 dBi at 2.8 deg.). [Blue] State 3 (Max Gain= 5.4 dBi at 11.25 deg.) and [Dark Gray] State 4 (Max Gain= 6.28 dBi at 22.5 deg.).

dielectric constant and loss tangent values of the Accura 60 substrate (see [54]). Fig. 4.5 shows the radiation pattern in the H-plane of the antenna for three states summarized in Table 4.1. A slight deviation of the steering angles from simulation for states 1 and 3 can be observed from Fig. 4.5. This can be attributed to the imprecise positioning of the cylinders and glass balls inside the channels. The total efficiency of the antenna at various states is summarized in Table 4.2. The maximum steering angle achieved from the prototype was 22.5°. Because of symmetry along the yz plane, the antenna would give a maximum steering angle of -22.5° if the cylinder and glass balls were moved towards the $+x$ direction, and therefore measurements were not repeated to demonstrate the negative angle.

4.4 Conclusions

The design of a parasitic patch array with beam steering capability was presented and discussed. It was demonstrated that the beam of the antenna can be steered $\pm$22.5° using a fluidic tuning technique. Measurement results show a return loss better than 10 dB and a maximum steering angle of 22.5° when metal cylinders and glass balls are moved in specific order in a certain direction. Movement of the cylinders and glass balls in the opposite direction will yield a steering angle of -22.5°. The antenna does not use any type of electronic components and is expected to be useful in systems that need to transmit signals with moderately high peak power levels (10s of Watts) while maintaining linearity.

Chapter 5

Power-Handling Study of Large-Scale Periodic Structures and Fluidically-Tunable Dual-Band Patch Antenna

5.1 Introduction

A significant body of research activities have primarily been focused on developing new design techniques and improving performances of periodic structures [29]. However, a detailed study of power-handling capability of periodic structures has not been done despite the promise these structures show in high-power applications. For example, B. A. Munk has addressed this issue and the limitation of power-handling capability of a certain type of periodic structure – frequency selective surfaces [5]. He points out that FSSs have limited power-handling capability due to two main reasons – dielectric breakdown and heat dissipation. This is in part due to the use of resonating elements as their building blocks. Inside a typical FSS, the local electric field intensity can be higher than that of the incident wave by several orders of magnitudes. He concluded that to improve the power handling capabilities of FSSs with resonant elements, the inter-element spacing should be as small as possible. However, in the case of FSSs populated with dipole-type elements, the inter-element spacing should not be reduced to a point where the tips of the elements are very close to each other. This close spacing will significantly enhance the electric field inside the structure, thereby reducing its power handling capability. Apart from the resonant element based FSSs, non-resonant element based FSSs proposed by our research group also exhibit limited power-handling capability due to the presence of metallic patches and wire grids. It has been shown that a miniaturized-element frequency selective surface (MEFSS) has no inherent advantage over a conventional FSS such

as Jerusalem Cross in terms of its power-handling capability [29]. However, detailed study done in our group has shown that the power-handling capability of an MEFSS can be increased by replacing the metallic capacitive patch layer with a high - ϵ_r substrate and modifying the geometry of the inductive layer [29]. As mentioned in chapter 2, there has been a growing demand in developing these type of periodic structures with agile frequency responses. The prominent technique to achieve tunable periodic structures has been the use of electronic components. However, electronic components exhibit non-linear behavior when exposed to high power electromagnetic waves/signals. This further deteriorates the power-handling capability of the periodic structures. This limitation has been demonstrated in [29] where two electronically tunable versions of the Galinstan based tunable MEFSS was designed, simulated and exposed to short-duration high-peak-power excitations. Similar limitation will also apply to patch antennas where electronic components are used to dynamically change the frequency, beam direction or polarization of the antennas.

In this chapter, power-handling capabilities of large-scale periodic structures and dual-band tunable patch antennas are studied and presented. The maximum power level that a periodic structure and/or antenna can handle depends on their exposure to the type of excitation signal i.e. continuous wave (CW) or transient. The power handling capability is limited by the failure of the material used in these structures. This failure is caused by two factors: heat dissipation and dielectric breakdown. With respect to the heat dissipation aspect, failure occurs when the structure operates under sustained high power levels. In such case, lossy materials will heat up and the surface will eventually melt or burn. On the contrary, dielectric breakdown occurs when the structure is exposed to very high peak power levels. In such case, the electric field strength in the dielectric material exceeds the break down level of the dielectric material. This failure typically occurs when short duration pulses with high peak power levels are transmitted.

Therefore, the aim of this study is to get an insight into the power handling capabilities, transient and CW, of large scale periodic structure and dual-band patch antenna in their designed and realized form as discussed in chapters 2 and 3. To achieve this goal, combined

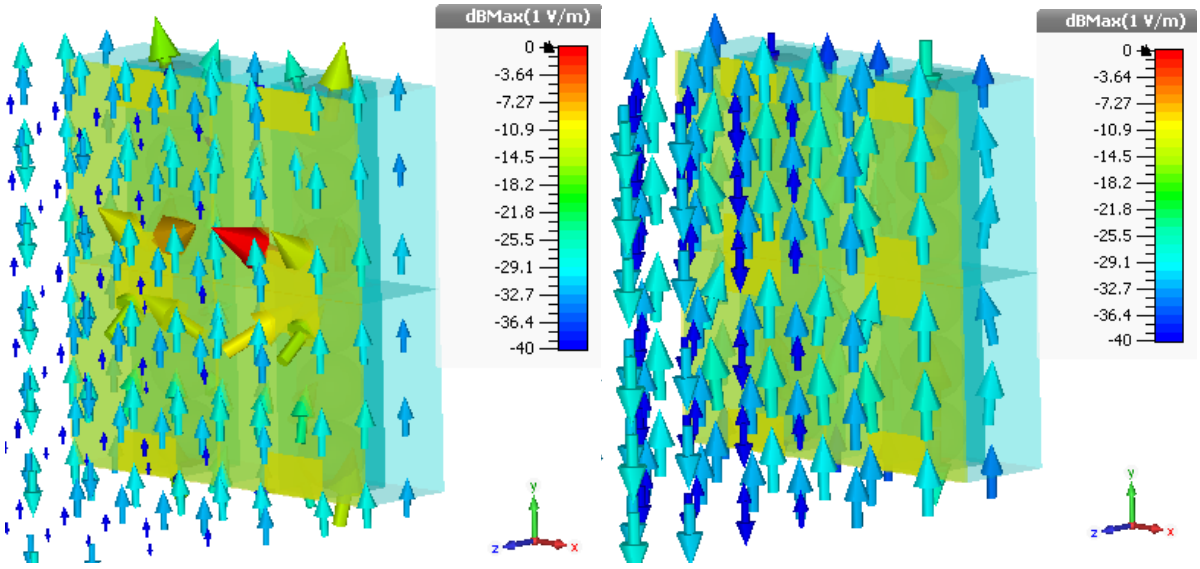

(a) (b)

Figure 5.1: Electric field distribution for the large scale periodic structure when (a) Glass ball is the center of the gap. (b) Glass ball is away from the gap [see Fig. 2.7(a)].

electromagnetic and thermal simulations in CST Microwave Studio are performed and results from the simulations are presented in the following sections.

5.2 Power-Handling Capability of Large-Scale Periodic Structure

In chapter 2, the proposed periodic structure consists of several capacitive patches fabricated on a dielectric substrate, which is then laid on top of a plastic substrate. The substrate is embedded with parallel channels populated with metal and glass balls. Due to the presence of metals, the local electric field intensity within the periodic structure can be significantly enhanced compared to the electric field intensity of the incident EM wave. Therefore, even a relatively low incident EM power level may cause high enough local electric field inside the periodic structure that can eventually cause to exceed the breakdown level of the structure. In order to estimate the amount of power (transient) that can cause breakdown of the structure, a systematic approach was followed and has been described here. First, the maximum electric

field value, two extreme points of the tunable frequency band, within the periodic structure unit cell was obtained from the full-wave simulation results (see Fig. 5.1). It should be noted here that the 6.0 mm unit cell structure was used for this analysis. As the breakdown voltage level of the Accura 60 substrate was unknown, air breakdown voltage level (3×10^6 V/m) had been used for convenience. It is known that power is proportional to the square of electric field. From the simulation, 1 watt (W) peak power generated 1.53×10^5 V/m inside the FSS. Considering air breakdown voltage level and the relation between power and electric field intensity, the periodic structure was estimated to be capable of handling a peak power level of around 385 W. For a periodic structure with multiple unit cells, the total peak power level can range from kilowatts (kW) to megawatts (MW).

Frequency: 9.59 (10.06) GHz

Incident e-field intensity (Max.): 3234 V/m

E-field intensity inside FSS (Max., for 1 W peak or 0.5 W rms power): 1.53×10^5 V/m (1.55×10^5 V/m)

Power (P) $\propto {E_{max}}^2$

P_{max} = $(3 \times 10^6)^2/(1.53 \times 10^5)^2$ = 385 W (374 W)

EM thermal co-simulation feature available in CST MWS was then used to study the CW power-handling capability of the large scale periodic structure. The thermal properties of Accura 60, mineral oil and glass beads were included in the simulation [53], [71]- [75]. To find out the approximate level of CW power, the power scaling factor in the thermal loss distribution dialog box was varied and simulation was run. This process was continued until a suitable power scaling factor was found which elevated the temperature of the structure close to the melting point of Accura 60 substrate. From the simulation of a unit cell, it had been determined that the periodic structure might be able to handle around 65 W rms power before the substrate would start to melt (melting point of the Accura 60 is $\approx$ 55°C - 65°C). Fig. 5.2 shows the thermal distribution on a unit cell of the periodic structure for a specific layout of the balls in the channel. It should be noted here that thermal transient solver had been used to estimate the amount of CW power.

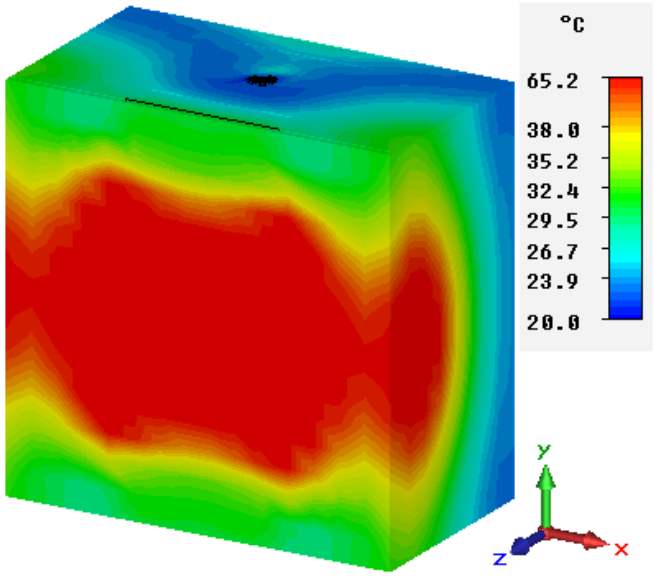

Figure 5.2: Temperature profile of a unit cell of the periodic structure when glass ball is at the center of the gap.

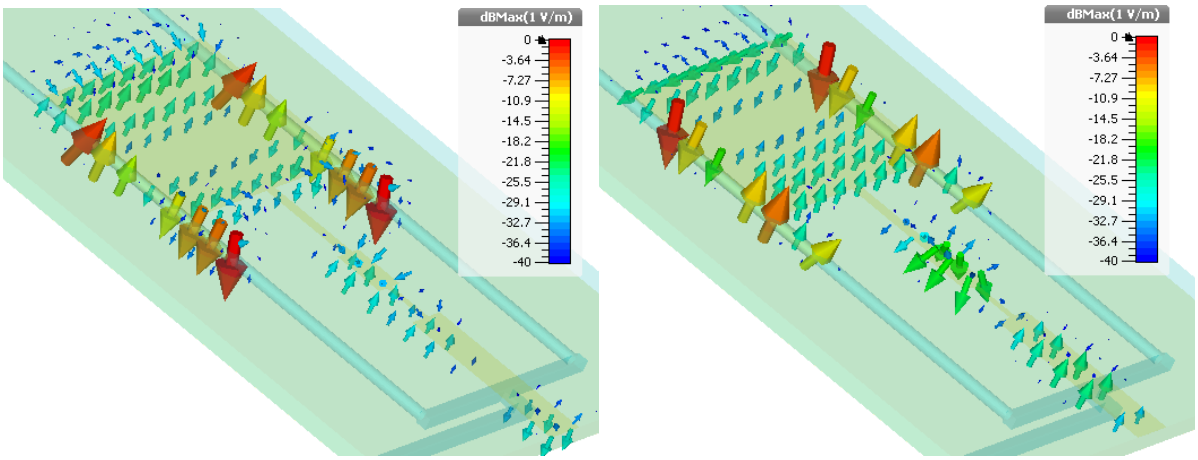

(a) (b)

Figure 5.3: Electric field distribution on the dual-band tunable patch antenna. (a) 2.37 GHz. (b) 2.88 GHz.

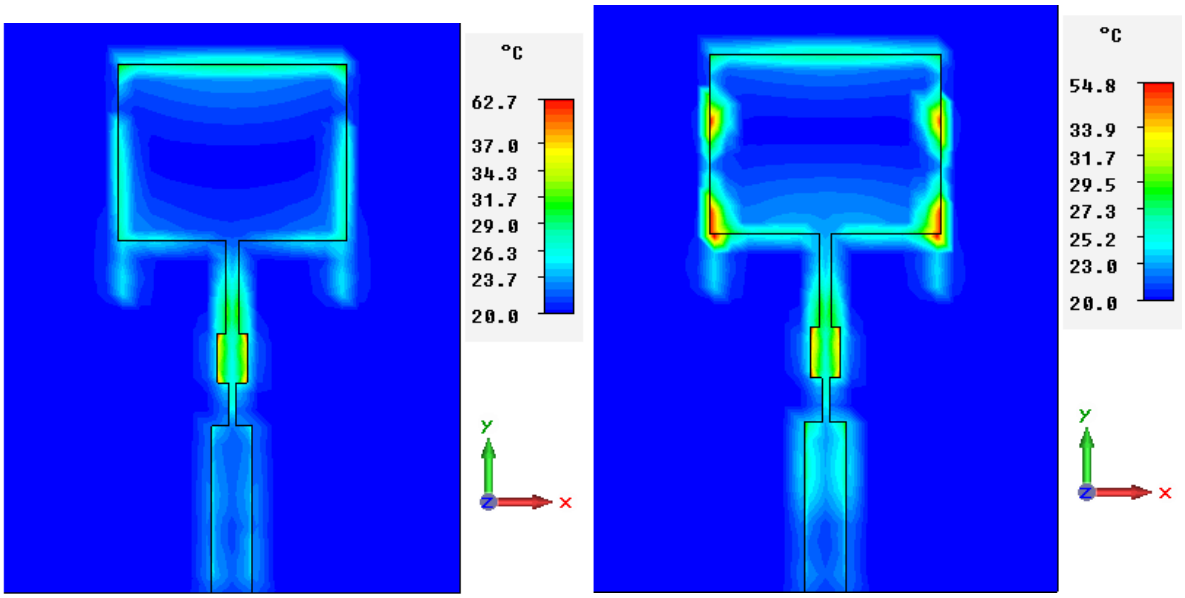

(a) (b)

Figure 5.4: Temperature profile of the patch antenna. (a) 2.37 GHz. (b) 2.88 GHz.

5.3 Power-Handling Capability of Tunable Dual-Band Patch Antenna

As described in chapter 3, the patch antenna consists of a substrate with embedded metal cylinders. Similar process as described in the previous section was followed to estimate the transient power-handling capability of the patch antenna. This study is limited only to one y_{offset} value, 23 mm (see Fig. 5.3).

Frequencies: 2.37 (2.88) GHz

Incident E-field intensity (Max.): 4865 V/m

E-field intensity inside patch antenna (Max.): 4.23×10^4 (4.18×10^4) V/m

Power (P) $\propto {E_{max}}^2$

P_{max} = $(3 \times 10^6)^2/(4.23 \times 10^4)^2$ = 5 kW (5.15 kW)

For the CW power-handling study, thermal transient analysis had been used as described in the previous section. From the simulation it had been determined that the antenna can

withstand $\approx$ 22 - 25 W rms power. Fig. 5.4 shows the temperature profile distribution of the patch antenna when y_{offset} = 23 mm.

5.4 Conclusions

A numerical study investigating the power handling capability of the fluidically tunable large-scale periodic structure and the dual band patch antenna from chapters 2 and 3 is presented. The power handling capability of both structures are limited by the failure of the materials used in them. Material failure occurs due to either dielectric breakdown or heat dissipation. The substrate used in these structures has a melting point of about 55°C - 65°C, which essentially limits the amount of CW and transient power that they can handle. Experimental validation is not performed as it is out of the scope of this thesis and has been left out as a topic for future investigation.

Chapter 6

Future Work and Conclusion

In the above chapters, a fluidic tuning technique has been applied in various microwave devices and their characteristics have been studied in detail. The technique shows promise in developing microwave devices that not only exhibit an agile response to various parameters but also capable of withstanding high power. However, future work based upon this thesis is still needed to continue the existing efforts and deliver a robust solution.

6.1 Future Work

The fluidic tuning mechanism was proposed by our group to design frequency selective surfaces with agile frequency responses. The proposed idea used liquid metal slugs and was demonstrated in unit cell configuration. The mechanism described in chapter 2 replaces liquid metal with solid balls and then with the use of 3D printing makes it possible to tune large scale periodic structures. This mechanism has been subsequently used in developing tunable microstrip antennas and described in chapters 3 and 4. However, the main obstacle arises in the fabrication process of 3D printed objects and has been described in chapter 2. With further progress in 3D printing technology and new material development, the issues can be minimized. In addition to that, fluidic tuning suffers from limited speed compared to electronic tuning. An accurate estimate of the tuning speed can be determined by using commercially available micropumps. Due to limitations posed by 3D printing technology, other means can be investigated to tune frequency responses and/or steer beam of periodic structures/antennas. One such way is to use mechanical system to move either the substrate or the elements (patch

in this case) or even the ground plane. For example, the patches can be fabricated on a thin substrate and then be moved rapidly using a mechanical system. The 3D printed substrate with populated balls will remain fixed in that situation. Alternatively, the ground plane of a structure can be moved horizontally or at an angle with respect to the substrate which will create a phase shift essentially steering the beam to a specific direction. Besides these, the patches can be fabricated on a flexible surface and then by mechanically bending the surface the frequency response of the structure can be tuned.

6.2 Conclusion

This thesis presents microwave devices such as periodic structures and microstrip antennas that can be fluidically reconfigured. A fluidic tuning technique was proposed by our research group to tune the frequency response of a frequency selective surface. However, the technique was demonstrated in a unit cell level and proved difficult to be implemented in a large scale structure. In this thesis, with the use of 3D printing technology, a symmetric pressure distribution network and solid metal balls it has been possible to implement a new technique that enables fluidic tuning of multi unit cell level periodic structure. Then applying the same concept, a single resonant patch antenna has been transformed into a dual-band one with tunable frequency response. In addition, with the help of this technique H-plane beam steering has been achieved for a 3-element mutually coupled patch antenna array. The responses of such type structures have also been demonstrated experimentally. During this process, it has also been shown the type of limitations 3D printing technology poses on the performance of these structures. Moreover, a power handling study for these devices is carried out and discussed in this thesis. Overall, the proposed fluidic tuning technique holds promise in developing reconfigurable microwave devices that are cost-effective and suitable for use in high-power applications.

DISCARD THIS PAGE

Appendix A: A Fluidic Colorimetric Sensor Design for Water Hardness Detection

A.1 Introduction

Water hardness is of great concern to both domestic and industrial users. It is caused by compounds of calcium and magnesium, and by a variety of other metals [76]. As the concentrations of calcium (Ca^{2+}) and magnesium (Mg^{2+}) are usually greater than other alkaline earth ions (Group 2), hardness is equated to [Ca^{2+}] + [Mg^{2+}] [77]. The amount of dissolved calcium and magnesium in water determines how hard the water is. Water hardness is typically classified into four types - soft (0-0.6 mmol/L), moderately hard (0.61-1.20 mmol/L), hard (1.21-1.80 mmol/L) and very hard ($\geq$ 1.81 mmol/L). For example, a big portion of the Great Plains and Mountain West in the US has 'very hard' water while the majority of the Southeast US has 'hard' water as seen in Fig. A.1 [78]. Hard water creates spot in glassware, build-up on pots, rings around the bathtub and toilet bowl and reduces efficiency of soap and detergents. Besides these, hard water also clogs pipes from households to industrial installations due to scale buildup which can lead to breakdowns and eventually costly repairs. In addition to all the above factors, too much calcium and magnesium in drinking water can be detrimental to human bodies [79]. Previous and current works in detecting water hardness include flow-batch photometric system [14], potentiometric sensor array [15], fluorescent molecular aptamer beacon [16], acoustic wave sensors [17] and so on. For example, the flow-batch photometric system uses the complexometric and colorimetric concepts but the system contains several components which need to be carefully integrated in order to perform the hardness screening. The proposed potentiometric sensor array system in [15] uses 7 ion-selective electrodes, a reference electrode and complex processing to determine calcium and total hardness of water. The electrodes used in the sensor array also have presence of multiple chemical substances. With all these factors taken into consideration, the above mentioned sensors may not be cost-effective and feasible to use in average households. Besides these, there are commercially available devices that can detect water hardness along with determining Ca^{2+} and Mg^{2+} concentration.

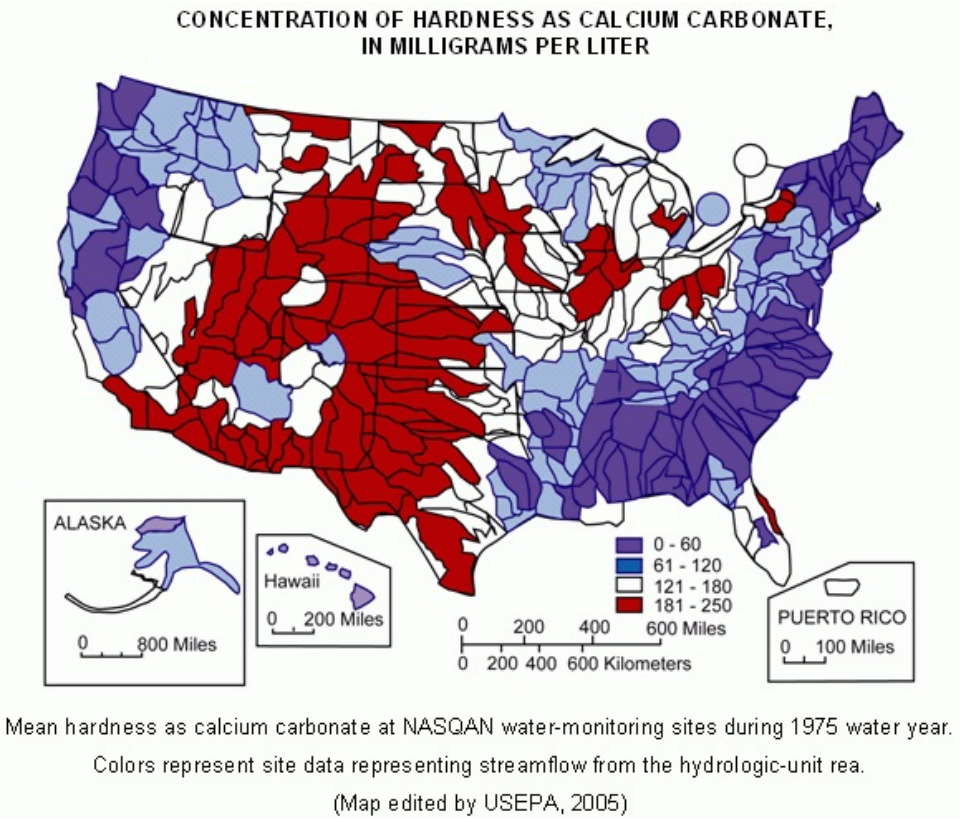

Figure A.1: Map of water hardness in USA as a concentration of $CaCO_3$ [78].

However, these devices are expensive, bulky in size and require additional configuration to use. The primary motivation behind this effort is to investigate a small-sized, low-cost sensor design that has the capability to integrate essential components of the detection system into single entity, can easily detect and determine water hardness (total hardness), robust and cost-effective for consumers.

In this chapter, we present a sensor that combines two well known concepts – complexometry and colorimetry to detect water hardness. Preliminary results on this have been reported in [80] and here we present detailed results on further work been done. A water sample is taken into a sensor prototype, which is 3D printed and mixed with a pH 10 buffer, a metal-ion indicator and finally titrated with a chelating ligand. A blue and a red Light-Emitting Diode (LED) are illuminated on one side of the prototype with two photodiodes being placed on the other side of it to sense the intensity of lights. During the mixing process, the color of the

solution changes prompting voltage variations across the two photodiodes. Therefore, visual observation of the water sample's color change and variation in voltage readings across the photodiodes confirm presence of Ca^{2+} and Mg^{2+} responsible for water hardness.

A colorimeter can be used to detect water hardness and also the concentration of calcium and magnesium ions in a sample. However, commercially available colorimeters are in the range of hundreds to thousands of dollars. There are also test kits available commercially that contain multiple items including chemicals required to perform water hardness test which can eventually become tedious and confusing. On the other hand, single and/or multiple LED and various types of detector based absorbance sensors are well investigated and summarized in [81]. Beside this, 3D printing is a rapidly growing technology and is capable of printing intricate structures. Our proposed design uses LEDs and photodiodes and integrates them into one unit with the help of 3D printing and printed relatively at a low price. It will thus eliminate the use and handling of multiple items and most importantly chemicals. Our proposed sensor is not intended to perform comprehensive water hardness detection but act as a redundant unit in existing systems. For instance, we are targeting household monitoring of water hardness, an example being water softener. The sensor may be used in average households where consumers can install it with their existing water softener system, a prospective application area. The sensor can then indicate whether the water is hard or soft just by checking the total hardness threshold value of soft water, which is around 0.6 mmol/L or 60 mg/L. Based on the information, the consumer can determine whether to replenish their water softener system or not. In the following sections, we discuss about the theory of complexometry and colorimetry, detailed experimental procedure and finally elaborate on the results.

A.2 Theory

Complexometry, also known as complexometric titration, is a titration based on complex formation [77]. Metal ions are Lewis acids, accepting electron pairs from electron-donating ligands that are Lewis bases [77]. When a ligand binds to a metal ion through more than one ligand atom, it is known as multidentate or chelating ligand. Ethylenediaminetetraacetic

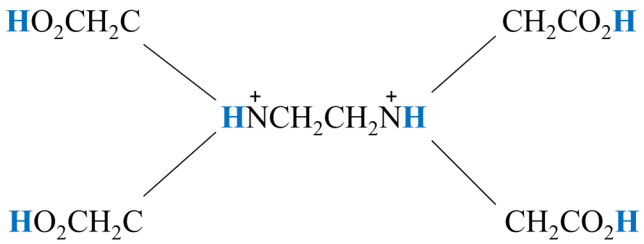

(a)

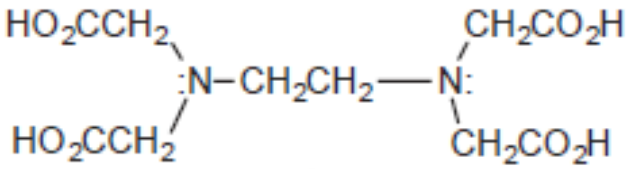

(b)

Figure A.2: EDTA - (a) Hexaprotic (b) Tetraprotic.

acid (EDTA) is a well-known chelating ligand or chelator. It is usually used as its disodium dihydrate salt [82]. It is a hexaprotic system designated by H_6Y^{2+}, where the highlighted acidic hydrogen atoms, Fig. A.2 (a), are lost upon metal-complex formation [77].

$$Ca^{2+} + Y^{4-} \longrightarrow CaY^{2-} \qquad K_f = 5.01 \times 10^{10} \tag{A.1}$$

$$Mg^{2+} + Y^{4-} \longrightarrow MgY^{2-} \qquad K_f = 4.9 \times 10^{8} \tag{A.2}$$

However, the neutral acid is tetraprotic and represented as H_4Y. EDTA forms strong complexes with nearly every metal ion carrying more than unit positive charge [82]. The stoichiometry for EDTA is 1:1, which means it binds to metal ions like Ca^{2+} and Mg^{2+} in a 1:1 ratio. The stability of a metal-EDTA complex is dependent on the pH of the solution. The complexes of divalent metals are stable in ammoniacal solution [82]. By varying pH of a solution, it can be decided which metals will be titrated with EDTA and which will not. For Ca^{2+} and Mg^{2+}, the complexation reaction with Y^{4-} and corresponding formation constants K_f are given by (A.1)

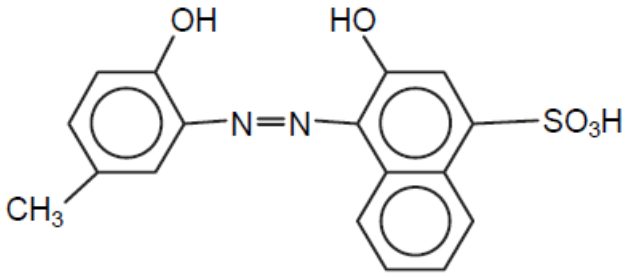

Figure A.3: Chemical structure of calmagite.

and (A.2) [83].

$$Ca^{2+} + HY^{3-} \longrightarrow CaY^{2-} + H^{+} \qquad K'_f = 1.8 \times 10^{10} \tag{A.3}$$

$$Mg^{2+} + HY^{3-} \longrightarrow MgY^{2-} + H^{+} \qquad K'_f = 1.7 \times 10^{8} \tag{A.4}$$

The formation constants with higher values mean that the above reactions will go to completion if EDTA exists in its completely deprotonated form. Moreover, the greater the stability of complexes the sharper the end points of the titration would be. To ensure that the titrant is in its completely deprotonated form, pH values greater than 12 are necessary [83]. However, at pH 12 both calcium and magnesium precipitate in the solution. Therefore, titration is generally carried out at pH 10 at which portion of EDTA is in HY^{3-} form and additional complexation reactions and conditional formation constants are given by (A.3) and (A.4) [83].

$$Mg^{2+} + HIn^{2-}(\text{blue}) \longrightarrow MgIn^{-}(\text{wine}-\text{red}) + H^{+} \tag{A.5}$$

[EDTA forms a weaker complex with Mg^{2+} than Ca^{2+}, Ca^{2+} reacts with EDTA first]

$$Ca^{2+} + MgIn^{-}(\text{wine}-\text{red}) + Y^{4-} \longrightarrow CaY^{2-} + MgIn^{-} \tag{A.6}$$

[After all Ca^{2+} is titrated, EDTA reacts with $MgIn^{-}$]

$$MgIn^{-}(\text{wine}-\text{red}) + Y^{4-} \longrightarrow MgY^{2-} + In^{3-}(\text{colorless}) \tag{A.7}$$

$$In^{3-}(\text{colorless}) + H_2O \longrightarrow HIn^{2-}(\text{blue}) + OH^{-} \tag{A.8}$$

Both EDTA and Ca^{2+} and Mg^{2+} ions are colorless. Therefore, a visual indication is needed to detect the end-point in EDTA titration. The most common technique is to use a metal ion indicator. Metal ion indicators are compounds whose color changes when they bind to a metal ion [77]. There are several metal ion indicators available such as Eriochrome black T, Calmagite, Murexide, Xylenol orange and Pyrocatechol violet. Useful indicators must bind metal less strongly than EDTA does [77]. Both Eriochrome black T and Calmagite have been used to detect water hardness. However, Calmagite provides a sharper end point and has a longer shelf life than Eriochrome black T [83]. 1-(2-Hydroxy-5-methyl-1-phenylazo)-2-napthanol-4-sulphonic acid or calmagite, Fig. A.3, was proposed as a general purpose metallochromic indicator, though principally for calcium and magnesium, by Diehl and Lindstrom [82]. When calmagite is added to a water sample at pH 10, it will react with the Ca^{2+} and Mg^{2+} and the color of the solution will turn into wine-red. As EDTA is added, it will first react with any free Ca^{2+} and Mg^{2+} and then start to react with the colored complex. EDTA will effectively remove the metal ions from the indicator and tightly bind with them. As the metal ions unbind from the indicator, the color of the solution starts changing to blue which also indicates the end point of the titration. It is worth mentioning that when magnesium content in the solution is low relative to the calcium content, magnesium/EDTA is added to aid in getting a sharper end point [82], [83]. Moreover, the indicator binds too weakly to the Ca^{2+} ions $(K'_f = 4.4 \times 10^3)$ and therefore to get a sharp end point Mg/EDTA is added into the solution [83]. The complete reaction process is given by (A.5) - (A.8) [84].

Spectrophotometry is any procedure that uses light to measure chemical concentrations [77]. Colorimetric analysis is adopted as it uses visible radiation to detect and determine the concentration of colored compounds in a solution. The intensity of light decreases as it passes through a solution. The amount of light passed through and absorbed by a solution is given by Transmittance (T) and Absorbance (A) respectively.

$$T = P/P_0 \tag{A.9}$$

$$A = log(P_0/P) = -logT \tag{A.10}$$

P_0 = Initial intensity and P = Final intensity of light.

Absorbance is related to the concentration of the sample, the path length that light has to cover and molar absorptivity of a particular substance. The relationship is expressed as Beers law and given as follows:

$$A = \epsilon bc \tag{A.11}$$

ϵ in molar absorptivity expressed in $M^{-1}cm^{-1}$, b is path length expressed in cm and c is concentration of the solution expressed in M (moles/liter).

A.3 Experimental Setup and Process

The prototype of the sensor was designed initially in Solidworks, a product of Dassault Systèmes SolidWorks Corporation located in Waltham, Massachusetts USA. Then it was printed using a 3D printer, Dimension Elite, which uses fused deposition modeling technology to print prototypes, Fig. A.4. The material used to print the prototype was Acrylonitrile Butadiene Styrene (ABS), a common thermoplastic. The overall dimension of the prototype was 30 mm $\times$ 40 mm $\times$ 15 mm. A 10 mm $\times$ 30 mm $\times$ 10 mm channel was embedded to hold the water sample. The prototype had two housings for two LEDs – one blue and one red, and two housings for two photodiodes. The path length that light had to cover in this prototype was 10 mm. A square opening was created for the photodiode housing and an iris was created for the LED

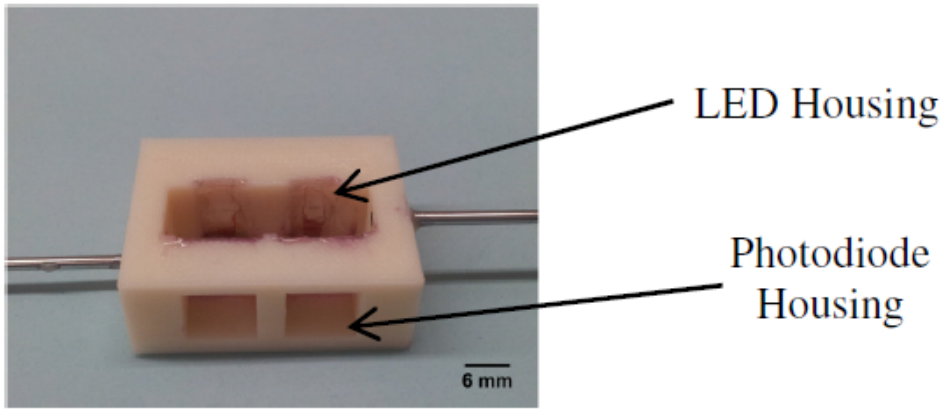

Figure A.4: 3D printed 1st generation prototype.

housing. All the openings were closed off with transparent plastic slides appropriately cut to the size of the openings. Then epoxy was applied between the slides and the prototype body to prevent any leakage of the sample. A circular inlet and an outlet were created to inject sample in and out of the channel.

Before the experiment, 20 drops of distill water were taken into a 30 cm^3 clean vial and a small scoop of calmagite powder was mixed at pH 10. The color of the solution turned blue indicating absence of Ca^{2+} and Mg^{2+} ions. The experiment was performed in a semi-dark room to prevent the photodiodes detecting external lights. Two LEDs were inserted into the LED housings and connected to two separate 9V batteries. Then two photodiodes were inserted into the housings and the leads were connected to one Fluke brand and one Agilent brand digital multimeters respectively. Water sample was collected from a tap and preserved in a clean plastic cup. Then using 5 ml syringe water was poured into the channel. The LEDs were turned on and the top portion of the channel, completely open, was covered with a plastic slide colored in black. The slide was assembled by pasting a black tape on one side of a plastic slide. Voltage readings were taken from the multimeters and recorded, 0.50 V and 0.46 V for blue and red light respectively. Then 2 drops of pH 10 buffer and 2 drops of unknown concentration of calmagite solution, prepared by mixing distilled water with calmagite powder, were poured into the channel using separate clean plastic pipets. As soon as the solution was mixed with the

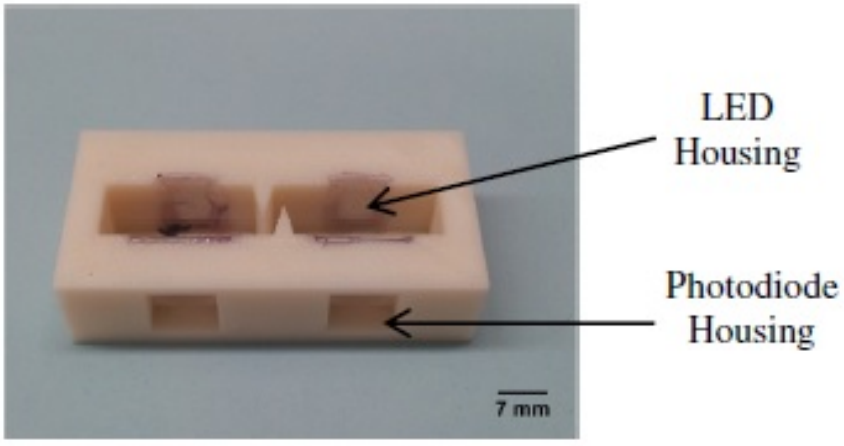

Figure A.5: 3D printed 2nd generation prototype.

water sample, it turned red. The top of the channel was covered with the black colored slide and voltage readings were recorded. The voltage across the photodiode detecting the blue light dropped by 0.11 V compared to the previous voltage reading whereas for the red light it only dropped by 0.03 V. After the measurement, the cover had been taken off and 2 drops of 0.2 M EDTA disodium salt (EDTA-Na_2) solution, purchased from Sigma-Aldrich, were added to the sample. As soon as the solution was mixed, the sample turned blue.The opening of the channel was covered with the black plastic and voltage readings were taken from the multimeters. The voltage reading for the photodiode detecting the red light dropped significantly to 0.21 V. On the other hand, the voltage reading for the blue LED jumped to 0.44 V. After the readings were recorded, the lights were turned off and the photodiodes and LEDs were carefully taken out of their housings. The sample solution was then discarded and the prototype was rinsed in cold water for few minutes. The prototype was then rinsed again with distilled water and finally wiped with a TechniCloth® II nonwoven wiper to avoid contamination and affecting later tests. The same process had been repeated 9 more times and finally the voltage readings were plotted with standard deviation error bars. Ten new tests were repeated at a later time with variation in one test parameter.

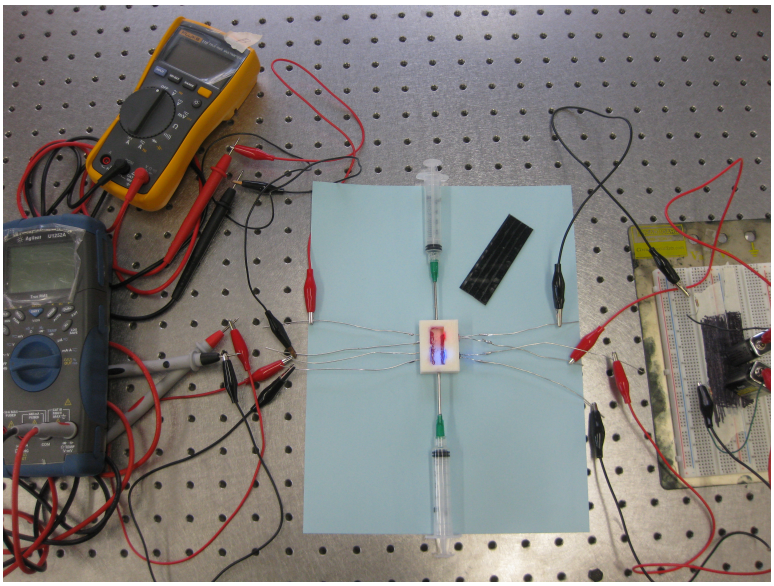

Figure A.6: Experimental configuration with 1st generation prototype.

Previously, an unknown concentration of calmagite was used whereas during these 10 new tests a known concentration, 0.005 M, of calmagite had been used. During these tests, 4 drops of calmagite were needed instead of 2 drops during the previous 10 sets of test. In the first prototype of the sensor, the housings for both photodiodes were placed in a close proximity. During the experiments, it was observed that light from one LED would also hit the other photodiode. This was due to the close proximity of the housings, internal reflection of light inside the channel and refraction caused by the printing material. Therefore, a second generation device was designed to minimize the light being detected by the other photodiode in addition to the photodiode placed right across a LED. The 2nd generation prototype was built using a Dimension Elite 3D printer with an overall dimension of 30 mm $\times$ 60 mm $\times$ 15 mm, Fig.

Table A.1: Transmittance and Absorbance (mean) of blue and red LED lights from 1st 10 sets and 2nd 10 sets of experiments with the 1st generation prototype respectively and finally 10 sets of experiment with the 2nd generation prototype holding sample (tap) water

	Transmittance (%)		**Absorbance**	
	Blue	***Red***	***Blue***	***Red***
Water, pH 10 buffer, Calmagite	78.848	92.509	0.104	0.034
Water, pH 10 buffer, Calmagite, EDTA	86.409	50.127	0.065	0.362
Water, pH 10 buffer, Calmagite	70.039	93.881	0.157	0.027
Water, pH 10 buffer, Calmagite, EDTA	86.529	25.618	0.063	0.616
Water, pH 10 buffer, Calmagite	78.702	92.954	0.104	0.032
Water, pH 10 buffer, Calmagite, EDTA	88.602	40.812	0.053	0.414

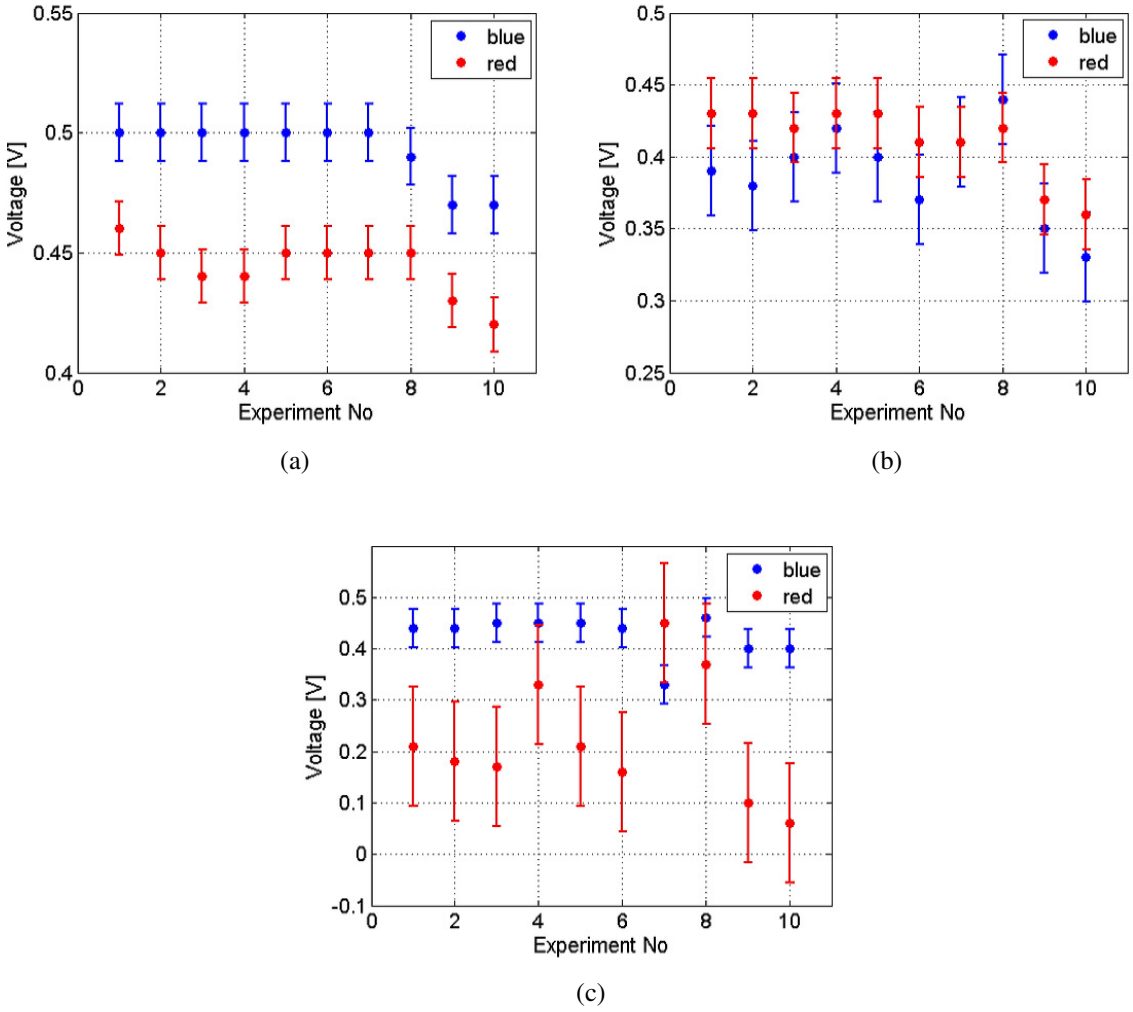

Figure A.7: Voltage reading with error bars across photodiodes from first 10 sets of experiment (a) with water sample only, (b) with water sample, pH 10 buffer & calmagite and (c) with water sample, pH 10 buffer, calmagite & EDTA for the 1st generation prototype.

A.5. It was printed using the same material as the 1st generation prototype, ABS. The inside channel of the prototype had a dimension of 10 mm $\times$ 50 mm $\times$ 12 mm. In the 2nd generation prototype, the input and output outlets were taken out, housings were placed apart by 16 mm and two wedge shaped blocks were placed in between the channel as a barrier for light to prevent detection by the other photodiode.

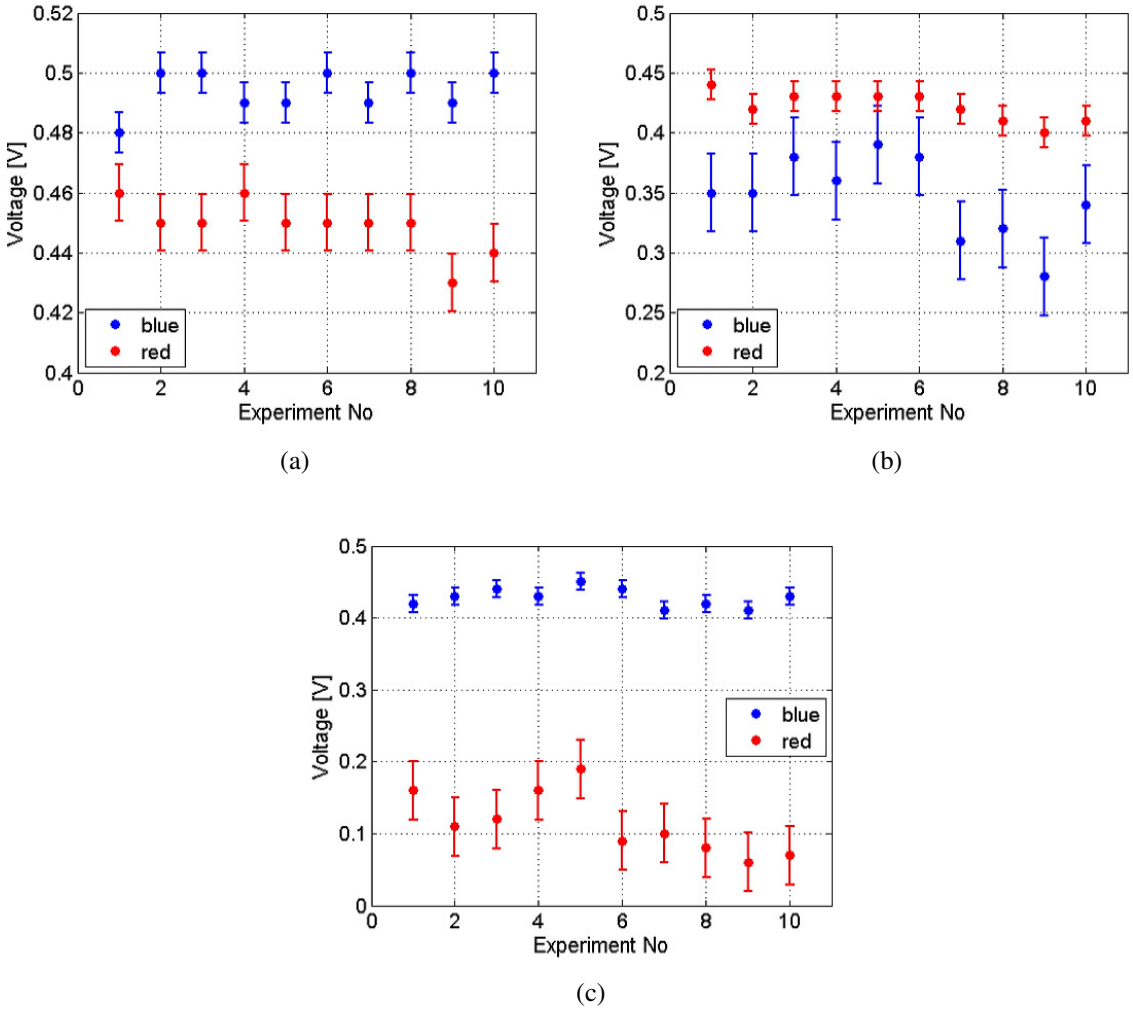

Figure A.8: Voltage reading with error bars across photodiodes from second 10 sets of experiment (a) with water sample only, (b) with water sample, pH 10 buffer & calmagite and (c) with water sample, pH 10 buffer, calmagite & EDTA for the 1st generation prototype.

The experimental setup for the second generation prototype was similar to the 1st generation setup as shown in Fig. A.6. Water sample was collected from a tap in the laboratory and stored in a plastic cup. Then water was poured into the channel with a 5 ml syringe and voltage readings were recorded for both photodiodes. Before the voltage reading was recorded, the top of the channel was covered with the black colored slide. The voltage readings for blue and red

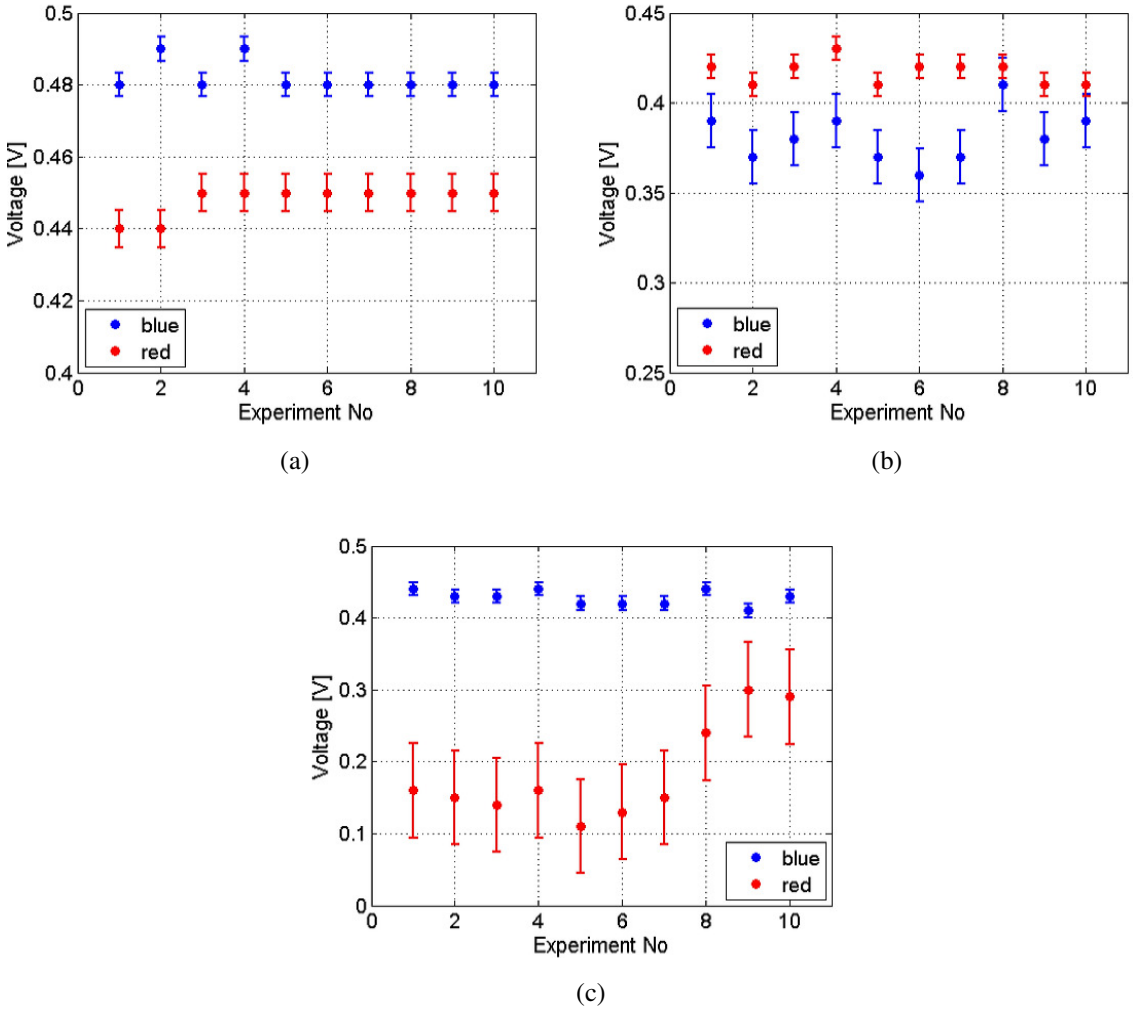

Figure A.9: Voltage reading with error bars across photodiodes from 10 sets of experiment (a) with water sample only, (b) with water sample, pH 10 buffer & calmagite and (c) with water sample, pH 10 buffer, calmagite & EDTA for the 2nd generation prototype.

light recorded were 0.48 V and 0.44 V respectively. Then the cover was taken off and 3 drops of pH 10 buffer and 4 drops of 0.005 M calmagite solution were added to the water sample. As soon as the solution was mixed it turned into red. The cover was put back again on top of the channel and voltage readings were observed and recorded. The voltage for the blue light dropped to 0.39 V in comparison to the previous reading. On the other hand, the voltage for

the red light dropped to 0.42 V, a change of 0.02 V only. After the readings were recorded, the cover was taken off again and 4 drops of 0.2 M EDTA solution were added to the water sample in the channel. The color then turned blue when EDTA was mixed with the sample. The voltage for the red light dropped by 0.26 V to 0.16 V whereas the voltage for the blue light jumped by 0.05 V. The sample was discarded and rinsed with cold water for few minutes. Then it was rinsed again with distill water to prepare it for another round of testing. The prototype was finally wiped with a TechniCloth® II nonwoven wiper and dried off. The process was repeated 9 additional times and color change was observed each time. After all tests were done, the voltage readings across the photodiodes were used to calculate transmittance and absorbance of the red and blue colored solution when calmagite and EDTA were added respectively. For example, transmittance of the red colored solution was calculated using equation (A.9) - dividing the recorded voltage data after calmagite was added to the mixture (sample water and pH 10 buffer) with the voltage data before calmagite was added to the mixture. Similarly, transmittance for blue colored solution was calculated by dividing the voltage data after EDTA was added to the mixture (sample water, pH 10 buffer and calmagite) with the voltage data of sample water and pH 10 buffer mixture. Finally the mean was computed from the transmittance values for each 10 sets of experiment. Absorbance was calculated from transmittance using equation (A.10) and the mean was then computed for each 10 sets of experiment. The mean transmittance and absorbance of the 1st 10 sets and 2nd 10 sets of experiments with the 1st generation device and 10 sets of experiment with the 2nd generation device are summarized in Table A.1.

After all the tests were done with the sample water, 0.1 - 1.1 milli-molar (mM) standard $CaCO_3$ solutions were prepared from a 2 mM standard solution of $CaCO_3$ by diluting it with distilled water. Then for each concentration (0.1 mM, 0.2 mM, 0.3 mM and so on) of the diluted $CaCO_3$ solution the transmittance and absorbance were calculated in the following way. The channel was partially filled up with standard 0.1 mM $CaCO_3$ solution. Then 4-6 drops of 0.3 mM $MgCl_2$ solution and 4-6 drops of pH 10 buffer were added to the solution. The top of the channel was covered with the black plastic cover and voltage readings across the

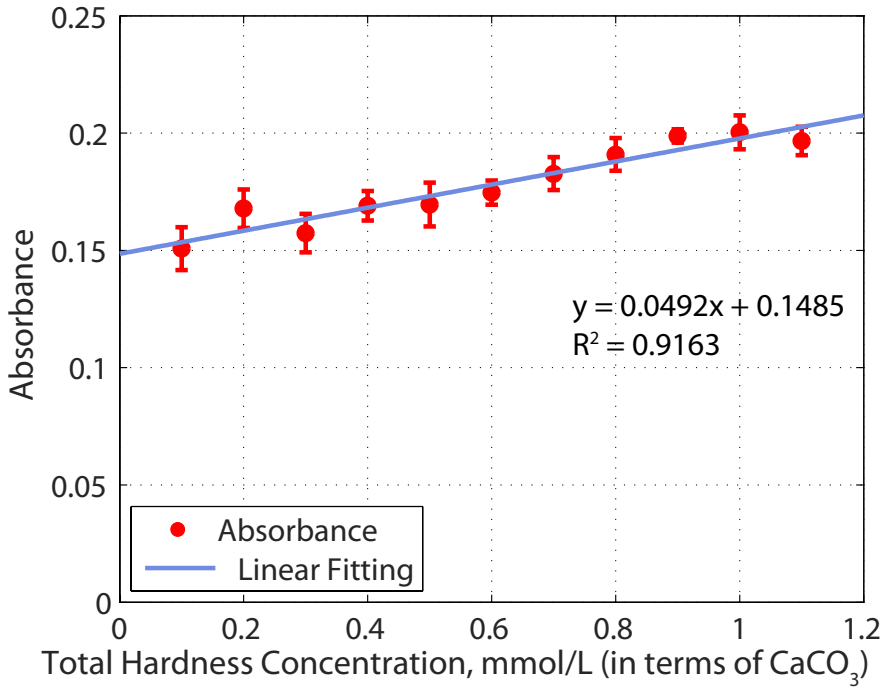

Figure A.10: Calibration data set obtained by using absorbance of red light after EDTA is added to solutions with different concentration of $CaCO_3$ (using the 2nd generation device).

photodiodes were recorded. Then after adding 3-5 drops of 0.005 M calmagite solution, the mixture turned red and voltage readings were recorded. Finally, 1-2 drops of EDTA were added to the mixture, which then turned blue and voltage readings were recorded. This whole process was repeated 4 additional times and for all the prepared diluted concentrations of $CaCO_3$. For concentration 0.7 mM and above, 8-9 drops of pH 10 buffer were mixed to the solution to observe color change when EDTA was added. Transmittance and absorbance were then computed in a similar fashion described earlier. The absorbance data for the red light was then used to form a calibration data set for our proposed sensor. Data from the experiments is shown and discussed in section A.4.

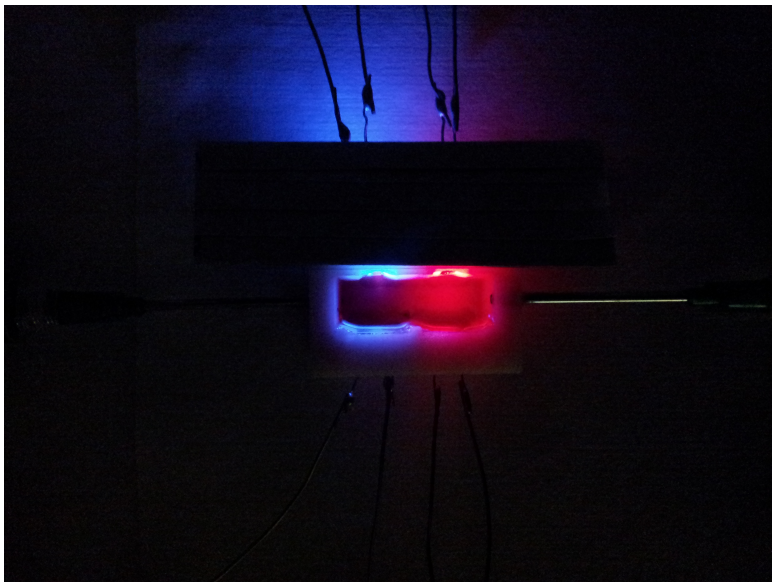

(a)

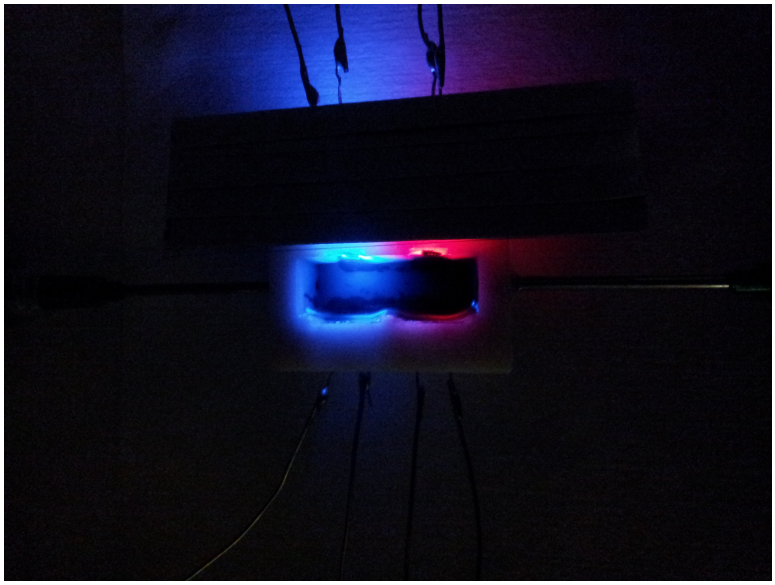

(b)

Figure A.11: (a) Red colored solution after calmagite is added and (b) Blue colored solution after EDTA is added to the water sample (using the 1st generation 3D printed prototype).

A.4 Results

Preliminary results on this work have been presented in [80]. Fig. A.7 and Fig. A.8 show the voltage readings with standard deviation error bars of the two photodiodes for two different

sets of 10 experiments respectively for the 1st generation 3D printed sensor prototype. The horizontal axis of the graphs represents the experiment number and vertical axis represents the voltage readings recorded by the multimeters across the two photodiodes. Fig. A.11 shows the color change when calmagite is added to the water sample at pH 10 and finally when EDTA is added to the sample. It should be noted that the black plastic cover was placed on top of the structure where the LEDs were located in order to prevent interference while capturing the picture. Fig. A.9 shows the voltage readings with standard deviation error bars of the two photodiodes for the 2nd generation sensor prototype. In Fig. A.9(c), the voltage readings for the red light are comparatively high for experiments 8-10; at least 0.08 V higher than the largest voltage drop among the first 7 experiments. The changes in the voltage drop caused the standard deviation error bar to become large compared to other measurements during the test. However, the overall trend on voltage drops from these 10 sets of experiment was comparable to the previous 20 sets of experiment with the 1st generation of prototype. The color change of the water sample during the experiments resembles the change during the first 20 sets of experiment for the 1st generation device, as seen in Fig. A.11(a)-(b), and hence not repeated here. From table A.1, the variation in transmittance and absorbance from each 10 sets of experiment has been relatively consistent. However, the transmittance for red light is relatively low, when solution is blue, compared to blue light, when solution is red. Fig. A.10 shows the calibration curve for the sensor with standard deviation error bars. As the concentration of $CaCO_3$ increases, the intensity of light detected by both the diodes decreases. The decreasing light intensity passing through the solution is thus captured by the gradual voltage variation across the photodiodes. The calibration data set is determined by taking into consideration the absorbance of red light when the solution turns blue after adding EDTA. Then basic curve fitting technique is used to plot the linear curve shown in Fig. A.10, which also shows the equation and R-squared term. As previously mentioned in section A.2, EDTA first reacts with any free Ca^{2+} and Mg^{2+} ions and then reacts with the colored metal-indicator complex. By comparing the absorbance data of the red light from the 2nd generation device holding tap

water with the calibration curve shown in Fig. A.10, it can be predicted that the sample (tap) water falls under the 'very hard' ($\geq$ 1.81 mmol/L) type water.

A.5 Conclusions

In this chapter, we have presented a sensor that detects hardness in water sample based on concepts of complexometric titration and colorimetric analysis. The sensor prototype has been designed using 3D printing technology which houses two LEDs, blue and red, and two photodiodes. A channel embedded in the prototype holds water sample. After calmagite is added to the sample it turns red prompting voltage drop at the photodiode detecting blue light. Then when EDTA is added to the solution it turns blue prompting voltage drop across the other photodiode. Therefore, we have shown through the experiments the presence of calcium and magnesium ions in the water sample, an indicator of water hardness. The 3D prototype is very shiny and reflects light internally and externally. Therefore, a new prototype has been designed to minimize light reflection. Experiments have been performed and similar trends in voltage readings across the photodiodes have been observed in comparison to the 1st generation prototype. Then a calibration curve has been obtained by measuring absorbance of various concentrations of $CaCO_3$ solution and from that curve the sample water's hardness has been predicted to be 'very hard'. As the concentration of solution increases, less light can pass through the solution causing gradual voltage drop. The gradual voltage drop thus indicates loss of transmittance, which in turn signifies the increase in absorbance.

The water hardness detection mechanism that we have discussed is based on observing color change of the solution and relating voltage drop due to the color change to absorbance of the solution. Our proposed sensor can be a cost-effective addition to existing water softener systems in average households, one possible application out of many, where it will check whether the water is soft or not just by checking the threshold concentration value, 0.6 mmol/L, of soft water. The sensor is not intended to perform a comprehensive and precise water hardness detection as sophisticated equipments exist in big installations such as city water supply

authority to perform rigorous and accurate detection and determination of water hardness. Future work will include choosing a dark colored 3D printing material to print the prototype, resizing the housings for both LEDs and photodiodes to prevent any misalignment, choosing a high resolution printer to avoid printing uneven surfaces and controlling test parameters more accurately. Besides these, a reliable mixing mechanism when pH 10 buffer, calmagite solution and EDTA are added to the water sample will be investigated. Presence of other metal ions such as copper, iron can interfere with water hardness detection. Therefore, techniques to neutralize the effect of other metal ions during water hardness detection will also be investigated. Even though calmagite solution is not deemed hazardous, a filtration option will be added to the sensor prototype in order to prevent mixing with the local sewage supply and causing further contamination.

Appendix B: List of Acronyms

FSS: Frequency Selective Surface

3D: Three Dimensional

RIS: Reactive Impedance Surface

AESA: Active Electronically Steerable Array

PESA: Passive Electronically Steerable Array

ESPAR: Electronically Steerable Parasitic Array Radiators

MEFSS: Miniaturized-Element Frequency Selective Surface

LED: Light Emitting Diode

EDTA: Ethylenediaminetetraacetic Acid

$CaCO_3$: Calcium Carbonate

$MgCl_2$: Magnesium Chloride

M: Molar

LIST OF REFERENCES

[1] Z. Zhang and S. Satpathy, "Electromagnetic Wave Propagation In Periodic Structures: Bloch Wave Solution Of Maxwells Equations," *Phys. Rev. Lett.*, vol. 65, issue 21, pp. 2650-2653, Nov. 1990.

[2] N. Stefanou *et al.*, "Scattering Of Electromagnetic Waves By Periodic Structures," *J. Phys.: Condens. Matter*, vol. 4, no. 36, pp. 7389-7400, 1992.

[3] F. Yang and Y. R. Samii, *Electromagnetic Band Gap Structures In Antenna Engineering*. New York: Cambridge University Press, 2009.

[4] T. J. Cui, D. R. Smith and R. Liu, *Metamaterials: Theory, Design And Application*. New York: Springer, 2010.

[5] B. A. Munk, *Frequency Selective Surfaces: Theory And Design*. New York: Wiley-Interscience, 2000.

[6] N. Behdad and M. Al-Joumayly, "A Generalized Synthesis Procedure For Low-Profile Frequency Selective Surfaces With Odd-Order Band-Pass Responses," *IEEE Trans. on Antennas and Propag.*, vol. 50, issue 6, pp. 1639-1643, Jun. 2008.

[7] N. Behdad and M. Al-Joumayly, "A Second-Order Band-Pass Frequency Selective Surface Using Non-Resonant Sub-Wavelength Periodic Structures," *Microw. and Optical Technology Lett.*, vol. 58, No. 7, pp. 2460-2464, Jul. 2010.

[8] D. Sievenpiper, L. Zhang, R. F. J. Broas, N. G. Alexopolous, and E. Yablonovitch, "High-Impedance Electromagnetic Surfaces With A Forbidden Frequency Band," *IEEE Trans. on Microw. Theory and Techniques*, vol.47, no.11, pp.2059-2074, Nov. 1999.

[9] B. A. Munk, *Finite Antenna Arrays And FSS*. New York: Wiley-Interscience, 2003.

[10] J. T. Bernhard, *Reconfigurable Antennas*. Morgan and Claypool, 2007.

[11] Hach. (2014, Nov. 6). Application - Water Hardness Guides [Online]. Available: http://www.hach.com/hardnessguide.

[12] Thermo Scientific. (2014, Nov. 6). Calcium Detection [Online]. Available: http://www.thermoscientific.com/content/tfs/en/products/calcium-detection-1.html.

[13] Libelium. (2014, Nov. 6). Smart Water Sensors To Monitor Water Quality In Rivers, Lakes And The Sea [Online]. Available: http://www.libelium.com/smart-water-sensors-monitor-water-quality-leakages-wastes-in-rivers-lakes-sea/.

[14] R. A. C. Lima *et al.*, "Hardness Screening Of Water Using A Flow-Batch Photometric System," *A. Chim. Acta*, vol. 518, iss. 1-2, pp. 25-30, Aug. 2004.

[15] J. Saurina, E. López-Aviles, A. Le Moal and S. Hernández-Cassou, "Determination Of Calcium And Total Hardness In Natural Waters Using A Potentiometric Sensor Array," *A. Chim. Acta*, vol. 464, iss. 1, pp. 89-98, Jul. 2002.

[16] T. Mairal Lerga and C. K. O'Sullivan, "Rapid Determination Of Total Hardness In Water Using Fluorescent Molecular Aptamer Beacon," *A. Chim. Acta*, vol.610, iss. 1, pp. 105-111, Mar. 2008.

[17] M. I. S. Veríssimo, J. A. B. P. Oliveira, and M. T. S. R. Gomes, "Determination Of The Total Hardness In Tap Water Using Acoustic Wave Sensors," *Sensors and Act. B: Chem.*, vol. 127, iss. 1, pp. 102-106, Oct. 2007.

[18] J. Nakajima *et al.*, "Hardness Indicator Composition And Method Of Water Hardness Analysis", U.S. Patent US6599748 B1, July 29, 2003.

[19] S. S. Sloat, "Eliminating Iron And Copper Ions", U.S. Patent US4205955 A, Jun. 3, 1980.

[20] H. Mitsumoto, "Hardness Measurement Reagent", U.S. Patent US7202090 B2, Apr. 10, 2007.

[21] Hach. (2014, Nov. 6). Total Hardness Test Kit, Model 5-B [Online]. Available: http://www.hach.com/total-hardness-test-kit-model-5-b/product?id=7640219508.

[22] Omega. (2014, Nov. 6). Water Quality Test Strips For pH, Alkalinity, Chlorine, Iron, Total Hardness, Iodine, Peroxide, Copper, Nitrate/Nitrite [Online]. Available: http://www.omega.com/pptst/WTS_Series.html.

[23] J. S. Fritz *et al.*, "Determination Of Total Hardness In Water Employing Visual And Spectrophotometric Titration Procedures," *Anal. Chem.*, vol. 41, no. 14, pp. 1954-1958, Dec. 1969.

[24] T. J. Brockett, "1D, 2D, and 3D Periodic Structures: Electromagnetic Characterization, Design, and Measurement," Ph.D dissertation, Dept. Elect. Eng., Univ. California Los Angeles, Los Angeles, CA, 2013.

[25] E. L. Pelton and B. A. Munk, "A Streamlined Metallic Radome," IEEE Trans. Antennas Propagat., vol. AP-22, pp. 799-803, Jun. 1974.

[26] L. C. Comtesse, R. J. Langley, E. A. Parker, and J. C. Vardaxoglou, "Frequency Selective Surfaces In Dual and Triple Band Offset Reflector Antennas," in 17th Eur. Microwave Conf., Rome, Italy, 1987, pp. 208-213.

[27] H. D. Griffiths, A. M. Vernon, and K. Milne, "Planar Phase Shifting Structures For Steerable DBS Antennas," Proc. 6th Int. Conf. on Antennas and Propag. (ICAP 89), 1989, pp. 45-49.

[28] T. R. Suresh Kumar, and C. Venkatesh, "Application Of Double Layer Frequency Selective Surface For SMPS Shielding," 2011 IEEE Int. Symp. on Electromagnetic Compatibility (EMC), 2011, pp.438-441.

[29] M. Li, "Tunable Frequency Selective Surfaces And True-Time-Delay Lenses For High-Power-Microwave (HPM) Applications," Ph.D dissertation, Dept. Elect. and Computer Eng., Univ. Wisconsin Madison, Madison, WI, 2013.

[30] D. F. Sievenpiper, "High-Impedance Electromagnetic Surfaces," Ph.D dissertation, Dept. Elect. Eng., Univ. California Los Angeles, Los Angeles, CA, 1999.

[31] S. Maci and G. B. Gentili, "Dual-Frequency Patch Antennas," *IEEE Antennas and Propag. Mag.*, vol. 39, no. 6, pp. 13-20, Dec. 1997.

[32] K. L. Wong and J. Y. Sze, "Dual-Frequency Slotted Rectangular Microstrip Antenna," *Electronic Lett.*, vol. 34, no. 14, pp. 1368-1370, Jul. 1998.

[33] K.L. Wong, *Compact and Broadband Microstrip Antennas*. New York: Wiley, 2002.

[34] C. Mias, "Varactor-Tunable Frequency Selective Surface With Resistive Lumped-Element Biasing Grids," *IEEE Microw. Wireless. Comp. Lett.*, vol. 15, pp. 570-572, 2005.

[35] A. C. Lima, E. A. Parker, and R. J. Langley, "Tunable Frequency Selective Surface Using Liquid Substrates," *Electron. Lett.*, vol. 30, pp. 281-282, 1994.

[36] W. Hu *et al.*, "Liquid Crystal Tunable mm-Wave Frequency Selective Surface," *IEEE Microw. Wireless. Comp. Lett.*, vol. 17, pp. 667700, Sep. 2007.

[37] J. M. Zendejas, J. P. Gianvittorio, Y. Rahmat-Samii, and J. W. Judy, "Magnetic MEMS Reconfigurable Frequency-Selective Surfaces," *J. Microelectromech. Syst.*, vol. 15, no. 3, pp. 613-626, 2006.

[38] M. Li, B. Yu and N. Behdad, "Liquid-Tunable Frequency Selective Surfaces," *IEEE Microw. Wireless. Comp. Lett.*, vol. 20, no. 8, pp. 423-425, Aug. 2010.

[39] M. Li and N. Behdad, "Fluidically Tunable Frequency Selective/Phase Shifting Surfaces For High-Power Microwave Applications," *IEEE Trans. Antennas Propag.*, vol. 60, pp. 2748-2759, Jun. 2012.

[40] S. V. Hum *et al.*, "Integrated MEMS Reflectarray Elements, in *Proc. Eur. Conf. Antennas Propag.*, Nov. 2006.

[41] C.-C. Cheng *et al.*, "A Programmable Lens-Array Antenna With Monolithically Integrated MEMS Switches, *IEEE Trans. Microw. Theory Tech.*, vol. 57, no. 8, pp. 1874-1884, Aug. 2009.

[42] J. B. L. Rao *et al.* , "Voltage-Controlled Ferroelectric Lens Phased Arrays, *IEEE Trans. Antennas Propag.*, vol. 47, pp. 458-468, Mar. 1999.

[43] L. Matekovits *et al.*, "Tunable Periodic Microstrip Structure On GAAS Wafer," *Prog. Electromag. Research*, vol. 70, pp. 1-10, 2009.

[44] B. J. Lei *et al.*, "A Wideband, Pressure-Driven, Liquid Tunable Frequency Selective Surface," *IEEE Microw. Wireless. Comp. Lett.*, vol. 21, pp. 465-467, Sep. 2011.

[45] Y. J. Sung, "Simple Tunable Dual-Band Microstrip Patch Antenna," *Electronic Lett.*, vol. 45, no. 13, pp. 666-667, Jun. 2009.

[46] Y. X. Guo, K. M. Luk, and K. F. Lee, "Dual-Band Slot-Loaded Short-Circuited Patch Antenna," *Electronic Lett.*, vol. 36, no. 4, pp. 289-291, Feb. 2000.

[47] J. Liang and H. Y. David Yang, "Microstrip Patch Antennas On Tunable Electromagnetic Band-Gap Substrates," *IEEE Trans. on Antennas and Propag.*, vol. 57, no. 6, pp. 1612-1617, Jun. 2009.

[48] Y. Sung, "A Switchable Microstrip Patch Antenna for Dual Frequency Operation," *ETRI J.*, vol. 30, no. 4, pp. 603-605, Aug. 2008.

[49] R. C. Hansen, *Phased Array Antennas*. Hoboken, NJ: Wiley, 2009.

[50] D. V. Thiel and S. Smith, *Switched parasitic antennas for cellular communications*. Massachusetts: Artech House, 2002.

[51] J. J. Luther, S. Ebadi and X. Gong, "A Microstrip Patch Electronically Steerable Parasitic Patch Array Radiator (ESPAR) Antenna With Reactance-Tuned Coupling And Maintained Resonance," *IEEE Trans. Antennas Propag.*, vol. 60, no. 4, pp. 1803-1812, Apr. 2012.

[52] D. Kim, D.W Lee, W. Choi, and J.B. Lee, "A Super-Lyophobic PDMS Micro-Tunnel As A Novel Microfluidic Platform For Oxidized Galinstan," in *2012 IEEE Int. Conf. MEMS*, Paris, 2012, pp. 1005-1008.

[53] Polysciences, Inc. (2012, Nov. 10). Glass Beads - Technical Data Sheet 857 [Online]. Available: http://cdnsm.polysciences.com/skin/frontend/default/polysciences/pdf/TDS%20857.pdf.

[54] S. Aguilar *et al.*, "Dielectric Characterization of PCL-Based Thermoplastic Materials For Microwave Diagnostic And Therapeutic Applications," *IEEE Trans. Biomedical Engineering*, vol. 59, pp. 627-633, Mar. 2012.

[55] C. G. Christodoulou, Y. Tawk, S. A. Lane and S. R. Erwin, "Reconfigurable Antennas For Wireless And Space Applications," *Proc. of IEEE*, vol. 100, no. 7, pp. 2250-2261, Jul. 2012.

[56] N. Haider, D. Caratelli and A. G. Yarovoy, "Recent Developments In Reconfigurable And Multiband Antenna Technology," *Int. Journal of Antennas and Propag.*, vol. 2013, pp. 1-14, Jan. 2013.

[57] F. Yang and Y. Rahmat-Samii, "A Reconfigurable Patch Antenna Using Switchable Slot For Circular Polarization Diversity," *Microw. and Wireless Comp. Letters*, vol. 12, issue 3, pp. 96-98, Aug. 2002.

[58] S. Xiao, B.Z. Wang and X.S. Yang, "A Novel Frequency-Reconfigurable Patch Antenna," *Microw. and Optical Tech. Letters*, vol. 36, issue 4, pp. 295-297, Feb. 2003.

[59] E. Erdil *et al.*, "Frequency Tunable Microstrip Patch Antenna Using RF MEMS Technology," *IEEE Trans. on Antennas and Propag.*, vol. 55, pp. 1193-1196, Apr. 2007.

[60] C. W. Jung, M.J. Lee, G. P. Li and F. D. Flaviis, "Reconfigurable Scan-Beam Single-Arm Spiral Antenna Integrated With RF-MEMS Switches," *IEEE Trans. Antennas Propag.*, vol. 54, pp. 455-463, Feb. 2006.

[61] N. Behdad and M. K. Sarabandi, "Dual-Band Reconfigurable Antenna With a Very Wide Tunability Range," *IEEE Trans. Antennas Propag.*, vol. 54, pp. 409-416, Feb. 2006.

[62] T. Bhattacharjee, H. Jiang and N. Behdad, "Large-Scale Fluidic Tuning of Sub-Wavelength Periodic Structures," *IEEE Antennas Wireless Propag. Lett.*, vol. 14, pp. 190-193, Feb. 2015.

[63] C. A. Balanis, "Microstrip Antennas," in *Antenna Theory Analysis and Design*, 3rd ed. New Jersey: Wiley-Interscience, 2005, ch. 14, pp. 811-876.

[64] R. Harrington, "Reactively controlled directive arrays," *IEEE Trans. Antennas Propag.*, vol. AP-26, pp. 390-395, May 1978.

[65] R. Schlub, J. Lu and T. Ohira, "Seven element ground skirt monpole ESPAR antenna design using a genetic algorithm and the finite element method," *IEEE Trans. Antennas Propag.*, vol. 51, no. 11, pp. 3033-3039, Nov. 2003.

[66] Y. Yusuf and X. Gong, "A low-cost patch antenna phased array with analog beam steering using mutual coupling and reactive loading," *IEEE Antennas Wireless Propag. Lett.*, vol. 7, pp. 81-84, 2008.

[67] H. Kawakami and T. Ohira, "Electrically steerable passive array radiator (ESPAR) antennas," *IEEE Antennas Propag. Mag.*, vol. 47, no. 2, pp. 43-49, Apr. 2005.

[68] D. Gray, W.L. Jun and D. V. Thiel, "Electronically steerable Yagi-Uda microstrip patch antenna array," *IEEE Trans. Antennas Propag.*, vol. 46, no. 5, pp. 605-608, May 1998.

[69] E. Van Lil and A. Van De Capelle, "Transmission line model for mutual coupling between microstrip antennas," *IEEE Trans. Antennas Propag.*, vol. 32, no. 8, pp. 816-821, Aug. 1984.

[70] D. Pozar, "Input impedance and mutual coupling of rectangular microstrip antennas," *IEEE Trans. Antennas Propag.*, vol. AP-30, no. 6, pp. 1191-1196, Nov. 1982.

[71] Industrial Glass Technologies. (2015, May 14). Soda-Lime-Silica Float Glass Selected Properties [Online]. Available: http://www.industrialglasstech.com/pdf/sodalimeproperties.pdf.

[72] 3D Systems. (2015, May 14). Accura 60 Technical Data [Online]. Available: http://www.3dsystems.com/sites/www.3dsystems.com/files/DS_Accura_60_US.pdf.

[73] Therminol. (2015, May 14). Therminol XP Heat Transfer Fluid [Online]. Available: https://www.therminol.com/products/Therminol-XP.

[74] C-Therm Technologies. (2015, May 14). Thermal Conductivity of Mineral Oil Based Transformer Fluid [Online]. Available: http://www.ctherm.com/blog/thermal_conductivity_of_mineral_oil_based_transformer_fluid.

[75] MultiTherm. (2015, May 14). Food Grade Mineral Oil MultiTherm PG-1 [Online]. Available: http://www.multitherm.com/multitherm-pg-1.html.

[76] Fairfax Water. (2013, Jul. 29). Explanation of Water Hardness [Online]. Available: http://www.fcwa.org/water/hardness.htm.

[77] D. C. Harris, *Quantitative Chemical Analysis*, 6th ed. New York: W. H. Freeman and Company, 2003.

[78] H. Perlman. (2013, Jul. 29). Water Properties And Measurements [Online]. Available: http://ga.water.usgs.gov/edu/characteristics.html

[79] World Health Organization. (2013, Jul. 1). Calcium And Magnesium In Drinking-Water: Public Health Significance [Online]. Available: http://whqlibdoc.who.int/publications/2009/9789241563550_eng.pdf.

[80] T. Bhattacharjee, H. Jiang and N. Behdad, "Sensor Design For Water Hardness Detection," in *2013 IEEE Sensors*, Baltimore, MD, 2013, pp. 1-4.

[81] M. O'Toole and D. Diamond, "Abosrbance Based Light Emitting Diode Optical Sensors And Sensing Devices," *Sensors*, vol. 8, iss. 4, pp. 2453-2479, Apr. 2008.

[82] T. S. West, *Complexometry With EDTA And Related Reagents*, 3rd ed. Poole, UK: BDH Chemicals Ltd, 1969.

[83] M. C. Yappert and D. B. DuPré, "Complexometric Titrations: Competition Of Complexing Agents In The Determination Of Water Hardness With EDTA," *J. Chem. Educ.*, vol. 74, no. 12, pp. 1422-1423, Dec. 1997.

[84] S. E. Bialkowski. (2013, Aug. 1). Titrimetric Water Hardness Determination [Online]. Available: http://ion.chem.usu.edu/∼sbialkow/classes/361/Hardness.html.